A Novel Transformation of the Ice Sheet Stokes Equations and Some of its Properties and Applications

John K. Dukowicz

Guest Scientist, Group T-3, Los Alamos National Laboratory,

Los Alamos, New Mexico, 87545, USA

Correspondence to: John K. Dukowicz (jn.dk@outlook.com)

Abstract.   We introduce a novel transformation of the Stokes equations into a form closely resembling the shallow Blatter-Pattyn equations. The two forms differ by only a few additional terms, while their variational formulations differ only by a single term in each horizontal direction. Specifically, the variational formulation of the Blatter-Pattyn model drops the vertical velocity in the second invariant of the strain rate tensor. Here we make use of the new transformation in two ways. First, we consider incorporating the transformed equations into a code that can be very easily converted from a Stokes to a Blatter-Pattyn model, and vice-versa, by switching these terms on or off. This may be generalized so that the Stokes model is switched on adaptively only where the Blatter-Pattyn model loses accuracy. Second, the key role played by the vertical velocity in the Blatter-Pattyn approximation motivates new approximations. Two examples are presented. These require a mesh that enables the discrete continuity equation to be invertible for the vertical velocity in terms of the horizontal velocity components. Examples of such meshes, such as the first order P1-E0 mesh and the second order P2-E1 mesh are given in both 2D and 3D. However, the transformed Stokes model has the same type of gravity forcing as the Blatter-Pattyn model, determined by the ice surface slope, thereby forgoing some of the mesh-generality of the traditional formulation of the Stokes model.

1 Introduction

Concern and uncertainty about the magnitude of sea level rise due to melting of the Greenland and Antarctic ice sheets have led to increased interest in improved ice sheet and glacier modeling. The gold standard is a Stokes model (i.e., a model that solves the nonlinear, non-Newtonian Stokes system of equations for incompressible ice sheet dynamics) because it is applicable to all geometries and flow regimes. However, the Stokes model is computationally demanding. It is a nonlinear, three-dimensional model involving four variables, namely, the three velocity components and pressure. The pressure is a Lagrange multiplier enforcing incompressibility and this creates a more

June 27, 2025

38 difficult indefinite "saddle point" problem. As a result, full-Stokes models exist but are

39 not commonly used in practice (examples are FELIX-S, Leng et al., 2012; Elmer/Ice,

40 Gagliardini et al., 2013).

42 Because of this there is much interest in simpler and cheaper approximate models.

43 There is a hierarchy of very simple models, such as the shallow ice (SIA) and shallow-

44 shelf (SSA) models, and there are also more accurate higher-order approximations.

45 These culminate in the Blatter-Pattyn (BP) approximation (Blatter, 1995; Pattyn, 2003),

46 which is currently used in production code packages such as ISSM (Larour et al., 2012),

47 MALI (Hoffman et al., 2018; Tezaur et al., 2015) and CISM (Lipscomb et al., 2019).

48 This approximation is based on the assumption of a small ice sheet aspect ratio, i.e.,

49 $\varepsilon = H/L \ll 1$, where H, L are the vertical and horizontal length scales, and consequently

50 it eliminates certain stress terms and implicitly assumes small basal slopes. Both the

51 Stokes and Blatter-Pattyn models are described in detail in Dukowicz et al. (2010),

52 hereafter referred to as DPL (2010). Although the Blatter-Pattyn model is reasonably

53 accurate for large-scale motions, accuracy deteriorates for small horizontal scales, less

54 than about five ice thicknesses in the ISMIP–HOM model intercomparison (Pattyn et al.,

55 2008; Perego et al., 2012), or below a 1 km resolution as found in a detailed comparison

56 with full Stokes calculations (Rückamp et al, 2022). This can become particularly

57 important for calculations involving details near the grounding line where the full

58 accuracy of the Stokes model is needed (Nowicki and Wingham, 2008). Attempts to

59 address the problem while avoiding the use of full Stokes solvers include variable mesh

60 resolution coupled with a Blatter-Pattyn solver (Hoffman et al., 2018) and variable model

61 complexity, where a Stokes solver is embedded locally in a lower order model (Seroussi

62 et al., 2012). Approximations that are more accurate than Blatter-Pattyn but cheaper than

63 Stokes are currently not available.

64

65 The present paper introduces two innovations that may begin to address some of

66 these issues. The first is a novel transformation of the Stokes model, described in §3,

67 which puts it into a form closely resembling the Blatter-Pattyn model and differing only

68 by the presence of a few extra terms. This allows a code to be switched over from Stokes

69 to Blatter-Pattyn, and vice-versa, globally or locally, by the use of a single parameter that

70 turns off these extra terms thus enabling variable model complexity to be very simply

71 implemented as described in §6.1. The second innovation is the introduction of new

June 27, 2025

72 finite element discretizations that decouple the discrete continuity equation and allow it to

73 be solved for the vertical velocity in terms of the horizontal velocity components.

74 Several elements used to construct such meshes are described in Appendix A in both 2D

75 and 3D, primarily the first order P1-E0 and second order P2-E1 elements (these two

76 elements are novel and are so-named because they employ pressures located on vertical

77 mesh edges). Within the framework of the transformed Stokes model these meshes

78 enable new approximations that surpass the Blatter-Pattyn approximation. We describe

79 two such approximations in §6.2. There is another very significant benefit. These new

80 meshes allow Stokes ice sheet models to be converted into inherently stable

81 unconstrained minimization problems without invoking the "inf-sup" condition as shown

82 in §4.3.2.

83

84 **2 The Standard Formulation of the Stokes Ice Sheet Model**

85 **2.1 The Assumed Ice Sheet Configuration**

86

87 An ice sheet may be divided into two parts, a part in contact with the bed and a floating

88 ice shelf located beyond the grounding line. The Stokes ice sheet model is capable of

89 describing the flow of an arbitrarily shaped ice sheet, including a floating ice shelf as

90 illustrated in Fig. 1, given appropriate boundary conditions (e.g., Cheng et al., 2020).

91 One limitation of the methods proposed here, in common with the Blatter-Pattyn model,

92 will be that there should be just one upper and one basal surface, as is the case in Fig. 1.

93 For simplicity we only consider fully grounded ice sheets with periodic lateral boundary

94 conditions although ice shelves can be incorporated.
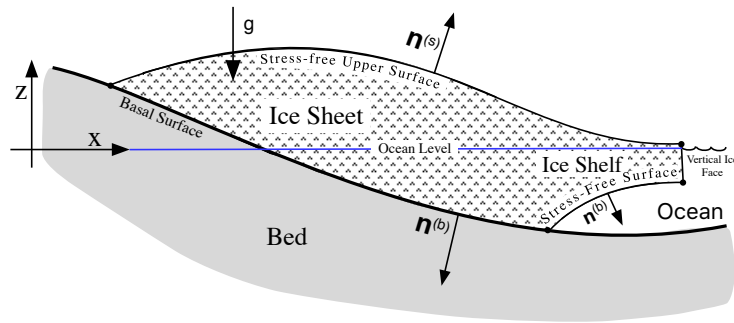
95
96
97 **Figure 1** A simplified illustration of the admissible ice sheet configuration.

98

99   Referring to Fig. 1, the entire surface of the ice sheet is denoted by S. An upper

100   surface, labeled S_s and specified by $\varsigma_s(x,y,z) = z - z_s(x,y) = 0$, is exposed to the

101   atmosphere and thus experiences stress-free boundary conditions. The bottom or basal

102   surface, denoted by S_B and specified by $\varsigma_b(x,y,z) = z - z_b(x,y) = 0$, is in contact with

103   the bed. The basal surface may be subdivided into two sections, $S_B = S_{B1} \cup S_{B2}$, where

104   S_{B1}, specified by $z = z_{b1}(x,y)$, is the part where ice is frozen to the bed (a no-slip

105   boundary condition), and S_{B2}, specified by $z = z_{b2}(x,y)$, is where frictional sliding

106   occurs. We assume Cartesian coordinates such that $x_i = (x,y,z)$ are position coordinates

107   with $z = 0$ at the ocean surface, and the index $i \in \{x,y,z\}$ represents the three Cartesian

108   indices. Later we shall have occasion to introduce the restricted index $(i) \in \{x,y\}$ to

109   represent just the two horizontal indices. This is more compact than the equivalent

110   projection operator, i.e., $u_{(i)} = P_i(u) = (u,v,0)$. Unit normal vectors appropriate for the

111   ice sheet configuration of Fig. 1 are given by

112

$$n_i = (n_x, n_y, n_z) = \frac{\partial \varsigma_s(x,y,z)/\partial x_i}{\left|\partial \varsigma_s(x,y,z)/\partial x_i\right|} = \frac{(-\partial z_s/\partial x, -\partial z_s/\partial y, 1)}{\sqrt{1 + (\partial z_s/\partial x)^2 + (\partial z_s/\partial y)^2}} \qquad \text{at surface } S_s,$$

$$n_i = (n_x, n_y, n_z) = -\frac{\partial \varsigma_b(x,y,z)/\partial x_i}{\left|\partial \varsigma_b(x,y,z)/\partial x_i\right|} = \frac{(\partial z_b/\partial x, \partial z_b/\partial y, -1)}{\sqrt{1 + (\partial z_b/\partial x)^2 + (\partial z_b/\partial y)^2}} \qquad \text{at surface } S_B.$$

(1)

113

114   **2.2 The Stokes Equations**

115

116   The Stokes model is a system of nonlinear partial differential equations and associated

117   boundary conditions (Greve and Blatter, 2009; DPL, 2010). In Cartesian coordinates the

118   Stokes equations, the three momentum equations and the continuity equation for the three

119   velocity components $u_i = (u,v,w)$ and the pressure P, are given by

120
$$\frac{\partial \tau_{ij}}{\partial x_j} - \frac{\partial P}{\partial x_i} + \rho g_i = 0 \,,$$
(2)

121
$$\frac{\partial u_i}{\partial x_i} = 0 \,,$$
(3)

122   where ρ is the density, and g_i is the acceleration vector due to gravity, arbitrarily

123   oriented in general but here taken to be in the negative z-direction, $g_i = (0,0,-g)$.

124   Repeated indices imply summation (the Einstein notation). The deviatoric stress tensor

125   τ_{ij} is given by

126
$$\tau_{ij} = 2\mu_n \dot{\varepsilon}_{ij} , \qquad (4)$$

127   where the strain rate tensor is

128
$$\dot{\varepsilon}_{ij} = \frac{1}{2}\left(\frac{\partial u_i}{\partial x_j} + \frac{\partial u_j}{\partial x_i} \right), \qquad (5)$$

129   the nonlinear ice viscosity μ_n is

130
$$\mu_n = \eta_0 \left(\dot{\varepsilon}^2 \right)^{(1-n)/2n} , \qquad (6)$$

131   and $\dot{\varepsilon}^2 = \dot{\varepsilon}_{ij}\dot{\varepsilon}_{ij}/2 \geq 0$ is the second invariant of the strain rate tensor that may be written

132   out in full as follows

133
$$\dot{\varepsilon}^2 = \frac{1}{2}\left[\left(\frac{\partial u}{\partial x}\right)^2 + \left(\frac{\partial v}{\partial y}\right)^2 + \left(\frac{\partial w}{\partial z}\right)^2 \right] + \frac{1}{4}\left[\left(\frac{\partial u}{\partial y} + \frac{\partial v}{\partial x}\right)^2 + \left(\frac{\partial u}{\partial z} + \frac{\partial w}{\partial x}\right)^2 + \left(\frac{\partial v}{\partial z} + \frac{\partial w}{\partial y}\right)^2 \right]. \qquad (7)$$

134   As usual, ice is assumed to obey Glen's flow law, where n is the Glen's law exponent

135   ($n = 1$ for a linear Newtonian fluid but typically $n = 3$ in ice sheet modeling, describing a

136   nonlinear non-Newtonian fluid). The coefficient η_0 is defined by $\eta_0 = A^{-1/n}/2$, where

137   A is an ice flow factor, in general depending on temperature and other variables (see

138   Schoof and Hewitt, 2013) but here taken to be a constant. The three-dimensional Stokes

139   system requires a set of boundary conditions at every bounding surface, each set

140   composed of three components. Aside from the periodic lateral boundary conditions, the

141   relevant boundary conditions are given as follows

142   (1) Stress-free boundary conditions on surfaces S_S not in contact with the bed, such

143   as the upper surface S_S:

144
$$\tau_{ij}n_j - Pn_t = 0 . \qquad (8)$$

145   (2) No-slip or frozen to the bed conditions on surface segment S_{B1}:

146
$$u_i = 0 . \qquad (9)$$

147   (3) Frictional tangential sliding conditions on surface segment S_{B2}:

June 27, 2025

148   We assume that the tangential frictional shear force that resists sliding, τ_i^S, is a known

149   vector that satisfies the no-penetration condition, $\tau_i^S n_i = 0$. Note that only two

150   components need to be provided since the third may always be obtained from the

151   tangency condition. In general τ_i^S is a complicated function of position and velocity

152   (e.g., Schoof, 2010). At a surface where frictional sliding takes place the flow velocity

153   must be tangential to the surface, satisfying

154
$$u_i n_i = 0. \tag{10}$$

155   Following DPL (2010), the tangential stress balance at the basal surface is given by

156
$$\tau_{ij} n_j - \tau_n n_i + \tau_i^S = 0, \tag{11}$$

157   where $\tau_n = n_i \tau_{ij} n_j$ is the normal component of the shear stress. However, the three

158   components of the stress balance (11) are not independent since the stress balance vector

159   is confined to the tangential plane. Thus, choosing the horizontal components of (11) as

160   the two independent components, the required three boundary conditions are given by the

161   no-penetration condition (10) and the two horizontal components of (11), namely

162
$$\tau_{(i)j} n_j - \tau_n n_{(i)} + \tau_{(i)}^S = 0. \tag{12}$$

163   In this paper we shall assume simple linear frictional sliding, given by

164
$$\tau_i^S = \beta(x) u_i, \tag{13}$$

165   where $\beta(x) > 0$ is a position-dependent drag law coefficient. We also assume that there

166   is no melting or refreezing at the bed, causing vertical inflows or outflows. If needed,

167   these can be easily added to (10) (see Dukowicz et al., 2010; Heinlein et al., 2022).

168

169   **2.3 The Stokes Variational Principle**

170

171   A variational principle, if available, is the most compact way of representing a particular

172   problem. It is fortunate that the Stokes model possesses a variational principle that is

173   particularly useful for discretization and for the specification of boundary conditions (see

174   Colinge and Rappaz (1999), Glowinski and Rappaz (2003), Rappaz and Reist (2005) for

175   early use of the variational principle in glaciology, and Schoof (2006), DPL (2010) for a

176   fuller description of the variational principle as applied in ice sheet modeling). There are

177   a number of significant advantages. For example, all boundary conditions are

178   conveniently incorporated in the variational formulation, terms in the variational

179 functional generally contain lower order derivatives, and the discretization automatically
180 generates a symmetric matrix. Stress terms are evaluated in the interior thereby avoiding
181 the need to evaluate derivatives using less accurate one-sided approximations at
182 boundaries. Stress-free boundary conditions, as at the upper surface, need not be
183 specified at all since they are automatically incorporated in the functional as natural
184 boundary conditions. Finally, functional variation in the discrete case is equivalent to
185 simple differentiation with respect to the discrete variables as demonstrated in §4. The
186 variational method presented here is closely related to the Galerkin method, a subset of
187 the weak formulation method in finite elements in which the test and trial functions are
188 the same (see Schoof, 2010, and earlier references contained therein in connection with
189 the Blatter-Pattyn model).

190

191 The variational functional for the standard Stokes model may be written in two
192 alternative forms:
193 (1) Basal boundary conditions imposed using Lagrange multipliers:

194
$$
\mathcal{A}[u_i, P, \lambda_i, \Lambda] = \int_V dV \left[\frac{4n}{n+1} \eta_0 \left(\dot{\varepsilon}^2 \right)^{(1+n)/2n} - P \frac{\partial u_i}{\partial x_i} + \rho g w \right]
$$
$$
+ \int_{S_{B1}} dS\, \lambda_i u_i + \int_{S_{B2}} dS \left[\Lambda u_i n_i + \frac{1}{2} \beta(x)\, u_i u_i \right],
$$
(14)

195 where λ_i and Λ are Lagrange multipliers used to enforce the no-slip condition and
196 frictional tangential sliding, respectively. As in DPL (2010), arguments enclosed in
197 square brackets, here $u_i, P, \lambda_i, \Lambda$, indicates the functions that are subject to variation.
198 (2) Basal boundary conditions imposed by direct substitution:
199 In case of no-slip conditions, condition (9) is used directly in the functional to zero out all
200 velocity components u_i along the S_{B1} section of the basal boundary. In case of
201 tangential sliding, the functional is given by

202
$$
\mathcal{A}[u_i, P] = \int_V dV \left[\frac{4n}{n+1} \eta_0 \left(\dot{\varepsilon}^2 \right)^{(1+n)/2n} - P \frac{\partial u_i}{\partial x_i} + \rho g w \right]
$$
$$
+ \frac{1}{2} \int_{S_{B2}} dS\, \beta(x) \left(u_{(i)} u_{(i)} + \left(u_{(i)} n_{(i)} / n_z \right)^2 \right),
$$
(15)

203 where, using the tangential sliding condition (10), the velocity along the entire basal
204 boundary section S_{B2} is specified by

June 27, 2025

205
$$u_i = \left(u, v, -u_{(i)} n_{(i)} / n_z\right) = \left(u, v, u_{(i)} \, \partial z_b / \partial x_{(i)}\right). \qquad (16)$$

206 This is implicitly done in all terms of the functional, i.e., the volume integral terms as
207 well as the surface integral term, in which case the replacement is explicitly visible in
208 (15). This use of (16) to replace the relevant surface velocities in the functional is
209 sufficient to implement the tangential sliding boundary condition. This replacement is
210 particularly easy in the discrete formulation, to be described later, where boundary or
211 surface velocity variables are easily accessible for replacement.
212
213   As described in DPL (2010), a variational procedure yields the full set of Euler-
214 Lagrange equations and boundary conditions that specify the standard Stokes model,
215 equivalent to (2)-(12). Using Lagrange multipliers, (14), the discrete variational
216 procedure determines the discrete variables that specify the velocity components and the
217 pressure, u_i, P, and the Lagrange multipliers, λ_i, Λ. In the direct substitution case, (15),
218 the solution determines only the discrete pressures P and velocity variables u_i that were
219 not directly prescribed as boundary conditions in (9) or (16). These prescribed (known)
220 values of boundary velocities are then added a posteriori to obtain the complete set of
221 discrete variables. The direct substitution method is smaller and simpler, and therefore
222 has been more commonly used in this paper.
223
224 **3. A Transformation of the Stokes Model**
225 **3.1 Origin of the Transformation**
226
227 The transformation is motivated by the Blatter-Pattyn approximation. Consider the
228 vertical component of the momentum equation and the corresponding stress-free upper
229 surface boundary condition in the Blatter-Pattyn approximation (from DPL, 2010, for
230 example), which are given by

231
$$\frac{\partial}{\partial z}\left(2\mu_n \frac{\partial w}{\partial z}\right) - \frac{\partial P}{\partial z} - \rho g = 0,$$
$$\left(2\mu_n \frac{\partial w}{\partial z} - P\right) n_z = 0 \quad \text{at} \quad z = z_s(x, y).$$
(17)

232 These equations suggest the use of a new variable $\tilde{P}$, to be called the transformed
233 pressure, given by

June 27, 2025

234
$$\tilde{P} = P - 2\mu_n \frac{\partial w}{\partial z} + \rho g\left(z - z_s(x,y)\right). \tag{18}$$

235 Using this, (17) simplifies as follows

236
$$\frac{\partial \tilde{P}}{\partial z} = 0, \tag{19}$$
$$\tilde{P} n_z = 0 \quad \text{at} \quad z = z_s(x,y),$$

237 which is a complete one-dimensional partial differential system that yields

238
$$\tilde{P} = 0 \tag{20}$$

239 when integrated from the top surface down. Thus, the transformed pressure vanishes in

240 the Blatter-Pattyn case. Replacing the pressure P by $\tilde{P}$ by the use of (18) forms the

241 basis of the present transformation. but we also make use of the continuity equation to

242 eliminate $\partial w/\partial z$ as in the Blatter-Pattyn approximation (e.g., Pattyn, 2003). Thus, the

243 transformation consists of eliminating P and $\partial w/\partial z$ in the Stokes system (2), (4)-(12)

244 (i.e., everywhere except in the continuity equation (3) itself) by use of

245
$$P = \tilde{P} - 2\mu_n\left(\frac{\partial u}{\partial x} + \frac{\partial v}{\partial y}\right) + \rho g\left(z_s - z\right), \tag{21}$$

246
$$\frac{\partial w}{\partial z} = -\left(\frac{\partial u}{\partial x} + \frac{\partial v}{\partial y}\right). \tag{22}$$

247

248 The pressure P in the standard Stokes system is primarily a Lagrange multiplier

249 enforcing incompressibility but with a very large hydrostatic component. The

250 transformed pressure $\tilde{P}$ again acts as a Lagrange multiplier enforcing incompressibility.

251 However, the transformation eliminates the hydrostatic pressure from $\tilde{P}$, making it some

252 three orders of magnitude smaller than P as illustrated in Fig. 2. Since $\tilde{P} = 0$ in the

253 Blatter-Pattyn approximation, the transformed pressure may be written as $\tilde{P} = P - P_{BP}$,

254 where

255
$$P_{BP} = -2\mu_n\left(\frac{\partial u}{\partial x} + \frac{\partial v}{\partial y}\right) + \rho g\left(z_s - z\right)$$

256 is the effective Blatter-Pattyn pressure (Tezaur et al., 2015). Thus, $P = P_{BP} + \tilde{P}$ and

257 therefore $\tilde{P}$ may be interpreted as the "Stokes" correction to the Blatter-Pattyn pressure.

258

June 27, 2025
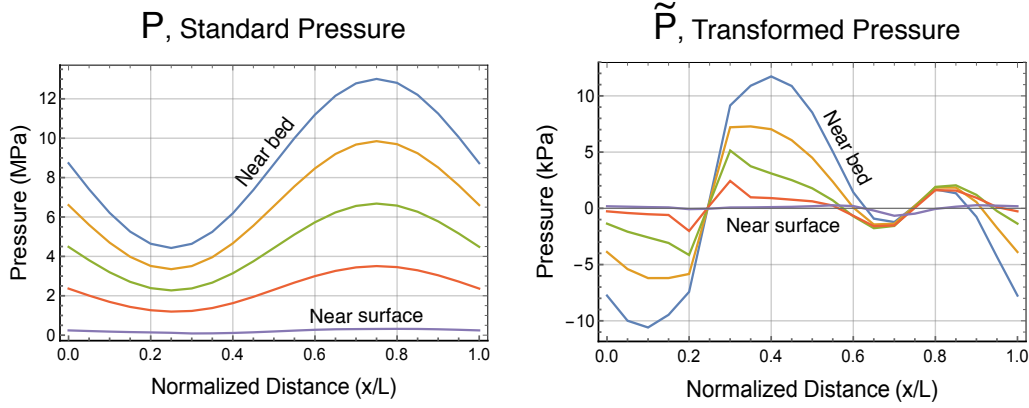
Figure 2. Standard pressure P (MPa) compared to the transformed pressure $\tilde{P}$ (kPa) in
 Exp. B from the ISMIP–HOM model intercomparison (Pattyn et al., 2008) at L = 10 km.

3.2 The Transformed Stokes Equations

Introducing (21), (22) into the Stokes system of equations (2)-(12) results in the
following transformed Stokes system:

$$\frac{\partial \tilde{\tau}_{ij}}{\partial x_j} - \hat{\xi}\frac{\partial \tilde{P}}{\partial x_i} - \rho g \frac{\partial z_s}{\partial x_{(i)}} = 0 \ , \tag{23}$$

$$\hat{\xi}\frac{\partial u_i}{\partial x_i} = 0 \ , \tag{24}$$

where quantities modified in the transformation are indicated by a tilde, e.g., $\tilde{P}$.

Corresponding to (4), the modified Stokes deviatoric stress tensor $\tilde{\tau}_{ij}$ is given by

$$\tilde{\tau}_{ij} = \tilde{\mu}_n \begin{bmatrix} 2\left(2\frac{\partial u}{\partial x}+\frac{\partial v}{\partial y}\right) & \left(\frac{\partial u}{\partial y}+\frac{\partial v}{\partial x}\right) & \left(\frac{\partial u}{\partial z}+\xi\frac{\partial w}{\partial x}\right) \\ \left(\frac{\partial u}{\partial y}+\frac{\partial v}{\partial x}\right) & 2\left(\frac{\partial u}{\partial x}+2\frac{\partial v}{\partial y}\right) & \left(\frac{\partial v}{\partial z}+\xi\frac{\partial w}{\partial y}\right) \\ \xi\left(\frac{\partial u}{\partial z}+\frac{\partial w}{\partial x}\right) & \xi\left(\frac{\partial v}{\partial z}+\frac{\partial w}{\partial y}\right) & 0 \end{bmatrix} \ , \tag{25}$$

Dummy variables $\xi, \hat{\xi}$ (here assumed to be $\xi, \hat{\xi} = 1$) have been introduced to indicate
terms that are absent in the Blatter-Blatter approximation, as will be more fully explained
below. The modified viscosity $\tilde{\mu}_n$, corresponding to (6), is given by

June 27, 2025

$$\tilde{\mu}_n = \eta_0 \left(\tilde{\dot{\varepsilon}}^2 \right)^{(1-n)/2n} , \qquad (26)$$

276   where the transformed second invariant $\tilde{\dot{\varepsilon}}^2$, corresponding to (7), is

$$\tilde{\dot{\varepsilon}}^2 = \left(\frac{\partial u}{\partial x} \right)^2 + \frac{\partial u}{\partial x}\frac{\partial v}{\partial y} + \left(\frac{\partial v}{\partial y} \right)^2 + \frac{1}{4}\left[\left(\frac{\partial u}{\partial y} + \frac{\partial v}{\partial x} \right)^2 + \left(\frac{\partial u}{\partial z} + \xi\frac{\partial w}{\partial x} \right)^2 + \left(\frac{\partial v}{\partial z} + \xi\frac{\partial w}{\partial y} \right)^2 \right]. \qquad (27)$$

278   Since (27) differs from (7) only by the incorporation of the continuity equation (22), the

279   transformation leaves both the second invariant $\tilde{\dot{\varepsilon}}^2$ and viscosity $\tilde{\mu}_n$ unchanged, i.e.,

280    $\tilde{\dot{\varepsilon}}^2 = \dot{\varepsilon}^2$ and $\tilde{\mu}_n = \mu_n$, which also implies that $\tilde{\dot{\varepsilon}}^2 \geq 0$.

281

282   Boundary conditions for the transformed equations, corresponding to (8)-(12), are

283   given by

284   BCs on S_S: $\qquad\qquad\qquad\qquad \tilde{\tau}_{ij}n_j - \hat{\xi}\tilde{P}n_i = 0$, $\qquad\qquad\qquad\qquad$ (28)

285   BCs on S_{B1}: $\qquad\qquad\qquad\qquad u_i = 0$, $\qquad\qquad\qquad\qquad$ (29)

286   BCs on S_{B2}: $\qquad\qquad\qquad\qquad u_i n_i = 0$, $\qquad\qquad\qquad\qquad$ (30)

287    $\qquad\qquad\qquad\qquad \tilde{\tau}_{(i)j}n_j - \tilde{\tau}_n n_{(i)} + \beta(x)u_{(i)} = 0$, $\qquad\qquad\qquad$ (31)

288   where $\tilde{\tau}_n = n_i\tilde{\tau}_{ij}n_j$ as before. Equations (30), (31) constitute the required three frictional

289   sliding boundary conditions.

290

291   As mentioned, dummy variables $\xi, \hat{\xi}$ in (23)-(25), (27), and (28) are used to

292   identify terms that are neglected in the two types of the Blatter-Pattyn approximation

293   discussed in §3.4. These are (a) the standard Blatter-Pattyn approximation, $\xi = 0, \hat{\xi} = 0$,

294   as originally derived (Blatter, 1995; Pattyn, 2003; DPL, 2010), which solves for just the

295   horizontal velocity components u, v, and (b) the extended Blatter-Pattyn approximation,

296    $\xi = 0, \hat{\xi} = 1$, described more fully in §3.4.2, that contains the standard approximation plus

297   additional equations that determine the vertical velocity w and the pressure $\tilde{P}$.

298   Retaining all terms, i.e., $\xi = 1, \hat{\xi} = 1$, specifies the full transformed Stokes model.

299

300   The transformed system, (23)-(31), and the standard Stokes system, (2)-(12),

301   produce exactly the same solution. However, in common with the Blatter-Pattyn

June 27, 2025

302 approximation, the transformed system requires the use a gravity-oriented coordinate

303 system because of the particular type of gravitational forcing being used, while the

304 standard Stokes model is not similarly restricted. This is not a major limitation.

305 Somewhat more restrictive is the appearance of $z_s(x, y)$, an implicitly single valued

306 function, to describe the vertical position of the upper surface of the ice sheet. This

307 means that care must be taken with reentrant upper surfaces (i.e., S-shaped in 2D) and

308 sloping cliffs at an ice edge, again a restriction that is not present in the standard Stokes

309 model. As noted earlier, we assume that there is just one upper and one basal surface,

310 i.e., as usual in ice sheet modeling this does not permit overhangs.

311

312 **3.3 The Transformed Stokes Variational Principle**

313

314 It is easy to verify that the transformed Stokes system (23)-(31) results from the variation

315 with respect to $u_i, \tilde{P}$ of the following functional:

$$
\begin{aligned}
\tilde{\mathcal{A}}[u_i, \tilde{P}] = \int_V dV &\left[\frac{4n}{n+1} \eta_0 \left(\tilde{\dot{\varepsilon}}^2 \right)^{(1+n)/2n} - \hat{\xi} \tilde{P} \frac{\partial u_i}{\partial x_i} + \rho g u_{(i)} \frac{\partial z_s}{\partial x_{(i)}} \right] \\
&+ \frac{1}{2} \int_{S_{B2}} dS\, \beta(x) \left(u_{(i)} u_{(i)} + \left(u_{(i)} n_{(i)} / n_z \right)^2 \right),
\end{aligned}
\tag{32}
$$

317 where $\tilde{\dot{\varepsilon}}^2$ is the transformed second invariant, (27). As in functional (15), here basal

318 boundary conditions are imposed by direct substitution. However, using Lagrange

319 multipliers as in (14) is also possible.

320

321 **3.4 Two Forms of the Blatter-Pattyn Approximation**

322 **3.4.1 The Standard Blatter-Pattyn Approximation**

323

324 The standard Blatter-Pattyn approximation (originally introduced by Blatter, 1995,

325 Pattyn, 2003; later by DPL, 2010; Schoof and Hewitt, 2013) is obtained by setting

326 $\xi = \hat{\xi} = 0$ in the transformed system. This yields the Blatter-Pattyn functional,

$$
\begin{aligned}
\mathcal{A}_{BP}[u_{(i)}] = \int_V dV &\left[\frac{4n}{n+1} \eta_0 \left(\dot{\varepsilon}_{BP}^2 \right)^{(1+n)/2n} + \rho g u_{(i)} \frac{\partial z_s}{\partial x_{(i)}} \right] \\
&+ \frac{1}{2} \int_{S_{B2}} dS\, \beta(x) \left(u_{(i)} u_{(i)} + \varsigma \left(u_{(i)} n_{(i)} / n_z \right)^2 \right),
\end{aligned}
\tag{33}
$$

June 27, 2025

328 and the second invariant

$$\dot{\varepsilon}_{BP}^2 = \left(\frac{\partial u}{\partial x}\right)^2 + \frac{\partial u}{\partial x}\frac{\partial v}{\partial y} + \left(\frac{\partial v}{\partial y}\right)^2 + \frac{1}{4}\left[\left(\frac{\partial u}{\partial y}+\frac{\partial v}{\partial x}\right)^2 + \frac{\partial u}{\partial z}^2 + \frac{\partial v}{\partial z}^2\right], \quad (34)$$

330 in terms of horizontal velocity components u,v only. The Euler-Lagrange equations and
331 boundary conditions are given by

$$\frac{\partial \tau_{(i)j}^{BP}}{\partial x_j} - \rho g\frac{\partial z_s}{\partial x_{(i)}} = 0; \quad \begin{cases} \tau_{(i)j}^{BP}n_j + \beta(x)\left(u_{(i)} + \zeta\left(u_{(j)}n_{(j)}/n_z\right)n_{(i)}/n_z\right) = 0 \\ \text{on } S_{B2}, \quad \tau_{(i)j}^{BP}n_j = 0 \text{ on } S_S, \quad u_{(i)} = 0 \text{ on } S_{B1}, \end{cases} \quad (35)$$

333 where the Blatter-Pattyn stress tensor $\tau_{(i)j}^{BP}$ is

$$\tau_{(i)j}^{BP} = \tilde{\mu}_n^{BP}\begin{bmatrix} 2\left(2\frac{\partial u}{\partial x}+\frac{\partial v}{\partial y}\right) & \left(\frac{\partial u}{\partial y}+\frac{\partial v}{\partial x}\right) & \frac{\partial u}{\partial z} \\ \left(\frac{\partial u}{\partial y}+\frac{\partial v}{\partial x}\right) & 2\left(\frac{\partial u}{\partial x}+2\frac{\partial v}{\partial y}\right) & \frac{\partial v}{\partial z} \end{bmatrix}, \quad (36)$$

335 and $\tilde{\mu}_n^{BP} = \eta_0\left(\tilde{\varepsilon}_{BP}^2\right)^{(1-n)/2n}$. A new dummy variable ζ has been introduced in (33) to
336 identify the basal boundary term normally dropped in the standard Blatter-Pattyn
337 approximation $(\zeta=0)$ but restored $(\zeta=1)$ in Dukowicz et al. (2011) to better represent
338 arbitrary basal topography.
339
340   The Blatter-Pattyn model solves for the horizontal velocity components only. In
341 principle the vertical velocity component w may be computed a posteriori by means of
342 the continuity equation, if desired. It is important to note that the Blatter-Pattyn system is
343 numerically well behaved because its variational formulation amounts to a convex
344 optimization problem whose solution minimizes the functional (33).
345
346 **3.4.2 The Extended Blatter-Pattyn Approximation**
347
348 A second form of the Blatter-Pattyn approximation is obtained from the transformed
349 variational principle (32) by making the assumption,

$$\left\|\frac{\partial w}{\partial x}\right\| \ll \left\|\frac{\partial u}{\partial z}\right\|, \quad \left\|\frac{\partial w}{\partial y}\right\| \ll \left\|\frac{\partial v}{\partial z}\right\|, \quad (37)$$

June 27, 2025

351 and therefore neglecting $\partial w/\partial x, \partial w/\partial y$ in the transformed second invariant $\tilde{\dot{\varepsilon}}^2$,

352 consistent with the original small aspect ratio approximation (Blatter, 1995; Pattyn, 2003;

353 DPL, 2010; Schoof and Hindmarsh, 2008). This corresponds to setting $\xi = 0, \hat{\xi} = 1$ in the

354 transformed Stokes model. In other words, we neglect w-velocity gradients in the

355 second invariant but keep the pressure term in the functional. This will be called the

356 extended Blatter-Pattyn approximation (EBP) because, in contrast to the standard Blatter-

357 Pattyn approximation, all the variables, i.e., $u, v, w, \tilde{P}$, are retained. It is noteworthy that

358 assumption (37) is equivalent to just setting $w = 0$ in the second invariant $\tilde{\dot{\varepsilon}}^2$ in the

359 transformed Stokes model. This will be exploited later to obtain approximations that

360 improve on the Blatter-Pattyn approximation. Thus, the extended Blatter-Pattyn

361 functional is given by

362
$$\mathcal{A}_{EBP}[u_i, \tilde{P}] = \int_V dV \left[\frac{4n}{n+1} \eta_0 \left(\dot{\varepsilon}_{BP}^2 \right)^{(1+n)/2n} - \tilde{P} \frac{\partial u_i}{\partial x_i} + \rho g u_{(i)} \frac{\partial z_s}{\partial x_{(i)}} \right]$$
$$+ \frac{1}{2} \int_{S_{B2}} dS\, \beta(x) \left(u_{(i)} u_{(i)} + \varsigma \left(u_{(i)} n_{(i)} / n_z \right)^2 \right), \tag{38}$$

363 where the Blatter-Pattyn second invariant $\dot{\varepsilon}_{BP}^2$ is given by (34). Taking the variation

364 yields the system of extended Blatter-Pattyn Euler-Lagrange equations and their

365 boundary conditions as follows

366   (1) Variation with respect to $u_{(i)}$ yields the horizontal momentum equation:

367
$$\frac{\partial \tau_{(i)j}^{BP}}{\partial x_j} - \frac{\partial \tilde{P}}{\partial x_{(i)}} - \rho g \frac{\partial z_s}{\partial x_{(i)}} = 0; \quad \begin{cases} \tau_{(i)j}^{BP} n_j - \tilde{P} n_{(i)} = 0 \text{ on } S_S, \quad u_{(i)} = 0 \text{ on } S_{B1}, \\ \tau_{(i)j}^{BP} n_j + \beta(x) \left(u_{(i)} + \varsigma \left(u_{(k)} n_{(k)} / n_z \right) n_{(i)} / n_z \right) = 0 \\ \qquad\qquad \text{on } S_{B2}, \end{cases} \tag{39}$$

368 where $\tau_{(i)j}^{BP}$ is given by (36).

369   (2) Variation with respect to w yields the vertical momentum equation:

370
$$-\frac{\partial \tilde{P}}{\partial z} = 0; \qquad \tilde{P} n_z = 0 \text{ on } S_S, \tag{40}$$

371   (3) Variation with respect to $\tilde{P}$ yields the continuity equation:

372
$$\frac{\partial w}{\partial z} + \frac{\partial u_{(i)}}{\partial x_{(i)}} = 0; \quad w = 0 \text{ on } S_{B1}, \text{ or } w = -u_{(i)} n_{(i)} / n_z \text{ on } S_{B2}. \tag{41}$$

373   It is apparent that the vertical momentum equation system (40) is a decoupled system,

374   yielding $\tilde{P} = 0$ as already shown in §3.1. This eliminates the pressure from the

375   horizontal momentum equation (39), making it identical to the standard Blatter-Pattyn

376   system (35), i.e., a decoupled system for the horizontal velocities $u_{(i)}$. As a result, having

377   solved (39) for the horizontal velocities, the continuity equation (41) may in principle be

378   solved for the vertical velocity w (but see the comments regarding the discrete case that

379   follow (42)).

380

381   In summary, the extended Blatter-Pattyn model, (39)-(41), is equivalent to the

382   standard Blatter-Pattyn model, (35), for the horizontal velocities, u, v, but it also includes

383   two additional equations determining the pressure $\tilde{P}$ and the vertical velocity w that are

384   ignored in the standard Blatter-Pattyn approximation. Because of this, we distinguish

385   between the *Blatter-Pattyn model* that solves for just the two horizontal velocities (i.e.,

386   the standard Blatter-Pattyn approximation, (35)), and the *Blatter-Pattyn system* that

387   solves for all the variables (i.e., the extended Blatter-Pattyn approximation, (39)-(41)).

388   Perhaps the main distinction between the two, which may be important in some

389   applications, is that in the Blatter-Pattyn system the continuity equation (41) is solved for

390   the vertical velocity w simultaneously with (39) for the horizontal velocities u, v on the

391   same mesh, while in the Blatter-Pattyn model the calculation of vertical velocity is

392   completely decoupled and may be done on an unrelated mesh. In the continuous case the

393   solution for the vertical velocity can be done using the Leibniz's theorem,

394
$$w(u,v) = w_{z=z_b} - \int_{z_b}^{z} \frac{\partial u_{(i)}}{\partial x_{(i)}} dz' = u_{(i)} \frac{\partial z_b}{\partial x_{(i)}} - \int_{z_b}^{z} \frac{\partial u_{(i)}}{\partial x_{(i)}} dz' = -\frac{\partial}{\partial x_{(i)}} \int_{z_b}^{z} u_{(i)} dz'. \qquad (42)$$

395   Equation (42) may in principle be discretized to obtain the vertical velocity on arbitrary

396   meshes. However, discretizations of the continuity equation (41) are generally not

397   capable of being solved for the vertical velocity in terms of the horizontal velocities. In

398   Appendix A we shall introduce special finite element meshes that do allow for the

399   solvability of the discrete continuity equation for the vertical velocity.

400

401   Up to now we have only dealt with continuum properties of Stokes-type systems,

402   which are well behaved. However, this may not be so in the discrete case. The solution

403   of the discretized Stokes systems will depend on the choices that are made for the meshes

404   and for the finite elements that are to be used. These issues will be discussed next.

405

June 27, 2025

4. Finite Element Discretization

4.1 Standard and Transformed Stokes Discretizations

In practice, both traditional Stokes and Blatter-Pattyn models are discretized using finite element methods (e.g., Gagliardini et al., 2013; Perego et al., 2012). We follow this practice except that here the discretization starts from the Stokes variational principle. This differs from standard finite element practice that begins with the Stokes equations and converts them into weak (integral) form, which may not be equivalent to a variational formulation unless the Galerkin method is used. A variational principle has a number of advantages (see §2.3 and DPL, 2010). The following is a brief outline of the discretization. Additional details are provided in Appendix A. For simplicity, we confine ourselves to two dimensions with coordinates (x,z) and velocities (u,w). An example of a three-dimensional mesh appropriate for our purpose is discussed in Appendix A. Further, we discuss only the case of direct substitution for basal boundary conditions in the variational functional. Remarks will apply to both the standard and the transformed Stokes models. Thus, the discrete pressure variable p may refer to either the standard pressure P or the transformed pressure $\tilde{P}$.

Consider an arbitrary mesh with a total of $N = n_u + n_w + n_p$ unknown discrete variables at nodal locations $1 \le i \le N$, with n_u horizontal velocity variables, n_w vertical velocity variables, and n_p pressure variables, so that

$$V = \left\{V_1, V_2, \cdots, V_N\right\}^T = \left\{\left\{u_1, u_2, \cdots, u_{n_u}\right\}, \left\{w_1, w_2, \cdots, w_{n_w}\right\}, \left\{p_1, p_2, \cdots, p_{n_w}\right\}\right\}^T = \left\{u, w, p\right\}^T \quad (43)$$

is the vector of unknown discrete variables that are the degrees of freedom of the model (if using Lagrange multipliers for basal boundary conditions then discrete variables corresponding to λ_z, Λ must be added). Variables are expanded in terms of shape functions $N_i^k(\mathbf{x})$ associated with each nodal variable i in each element k, so that

$V^k(\mathbf{x}) = \sum_i V_i N_i^k(\mathbf{x})$ is the spatial variation of variables in element k, summed over all variable nodes located in element k. Shape functions associated with a given node may differ depending on the variable. Substituting into the functional, (15) or (32), integrating and assembling the contributions of all elements, we obtain a discretized variational functional in terms of the nodal variable vectors u, w, p, as follows

June 27, 2025

$$\mathcal{A}(u,w,p) = \sum_k \mathcal{A}^k(u,w,p), \tag{44}$$

where $\mathcal{A}^k(u,w,p)$ is the local functional evaluated by integrating over element k. Since the product of pressure and the divergence of velocity in the functional is linear in pressure and velocity, and the term responsible for gravity forcing is linear in velocity, the functional (44) may be written in discrete form as follows

$$\mathcal{A}(u,w,p) = \mathcal{M}(u,w) + p^T\left(\mathbf{M}_{UP}^T u + \mathbf{M}_{WP}^T w\right) + u^T F_U + w^T F_W, \tag{45}$$

where the notation from (43) has been used, i.e., $u = \left\{u_1, u_2, \cdots, u_{n_u}\right\}^T$, etc. Parentheses indicate a functional dependence on the indicated variables. Comparison with (15) and (32) shows that $\mathcal{M}(u,w) \geq 0$ is a highly nonlinear function of the velocity variables u, w, and $\mathbf{M}_{UP}^T, \mathbf{M}_{WP}^T$ are constant $n_p \times n_u$ and $n_p \times n_w$ matrices, respectively, arising from the incompressibility constraint. Note that F_U, F_W are constant gravity forcing vectors of dimension n_u and n_w, respectively, such that $F_U = 0, F_W \neq 0$ in the standard Stokes model, and $F_U \neq 0, F_W = 0$ in the transformed Stokes model. The discrete functional $\mathcal{M}(u,w)$ differs but it remains positive-definite in the two cases.

Variation of the discretized functional corresponds to partial differentiation with respect to each of the discrete variables in the vector V (see (43)). Thus, the discrete Euler-Lagrange equations that correspond to the u-momentum, w-momentum, and continuity equations, respectively, are given by

$$R(u,w,p) = \begin{bmatrix} \partial\mathcal{A}(u,w,p)/\partial u \\ \partial\mathcal{A}(u,w,p)/\partial w \\ \partial\mathcal{A}(u,w,p)/\partial p \end{bmatrix} = \begin{bmatrix} R_U(u,w,p) \\ R_W(u,w,p) \\ R_P(u,w) \end{bmatrix} = \begin{bmatrix} \mathcal{M}_U(u,w) + \mathbf{M}_{UP}p + F_U \\ \mathcal{M}_W(u,w) + \mathbf{M}_{WP}p + F_W \\ \mathbf{M}_{UP}^T u + \mathbf{M}_{WP}^T w \end{bmatrix} = 0, \tag{46}$$

where functionals $\mathcal{M}_U(u,w) = \partial\mathcal{M}(u,w)/\partial u$, $\mathcal{M}_W(u,w) = \partial\mathcal{M}(u,w)/\partial w$ are nonlinear vectors of dimension n_u and n_w, respectively. Altogether, (46) is a set of N nonlinear equations for the N unknown discrete variables V_i. As explained previously in the continuum case, all boundary conditions are included in functional (45) and therefore they are also incorporated in the discrete Euler-Lagrange equations (46).

June 27, 2025

462

463   Since the overall system (46) is nonlinear, it is normally solved using Newton-

464 Raphson iteration, expressed in matrix notation as follows

$$\mathbf{M}\left(u^K, w^K\right)\Delta V + R\left(u^K, w^K, p^K\right) = 0 , \qquad (47)$$

465

466 where K is the iteration index, $\mathbf{M}(u,w) = \partial^2 \mathcal{A}(V) / \partial V_i \partial V_j$ is a symmetric $N \times N$

467 Hessian matrix, and ΔV is the column vector given by

$$\Delta V = \left\{\Delta u, \Delta w, \Delta p\right\}^T = \left\{u^{K+1} - u^K, w^{K+1} - w^K, p^{K+1} - p^K\right\}^T .$$

468

469 Given V^K from the previous iteration, (47) is a linear matrix equation that is solved for

470 the N new variables V^{K+1} at each iteration. In view of (45) and (46), the Hessian matrix

471 $\mathbf{M}(u,w)$ may be decomposed into submatrices as follows

$$\mathbf{M}(u,w) = \begin{bmatrix} \mathbf{M}_{UU}(u,w) & \mathbf{M}_{UW}(u,w) & \mathbf{M}_{UP} \\ \mathbf{M}_{UW}^T(u,w) & \mathbf{M}_{WW}(u,w) & \mathbf{M}_{WP} \\ \mathbf{M}_{UP}^T & \mathbf{M}_{WP}^T & 0 \end{bmatrix} . \qquad (48)$$

472

473 Submatrices $\mathbf{M}_{UW}(u,w) = \partial^2 \mathcal{M}(u,w) / \partial u \partial w$, etc., depend nonlinearly on u, w. Thus,

474 $\mathbf{M}_{UU}(u,w), \mathbf{M}_{WW}(u,w)$ are square $n_u \times n_u$, $n_w \times n_w$ symmetric matrices, respectively,

475 while $\mathbf{M}_{UW}(u,w)$ is a rectangular $n_u \times n_w$ matrix since in general n_u, n_w are not equal.

476 As noted earlier, $\mathbf{M}_{WP}^T$ is an $n_p \times n_w$ matrix that is not square unless $n_p = n_w$.

477

478 **4.2 Blatter-Pattyn Discretizations**

479

480 For completeness, we express the two Blatter-Pattyn approximations from §3.4 in

481 discretized form from §4.1, as follows

482   (1) The standard Blatter-Pattyn model from §3.4.1 takes the simple form

$$R_U\left(u,0,0\right) = \mathcal{M}_U\left(u,0\right) + F_U = 0 , \qquad (49)$$

483

484 whose Newton-Raphson iteration is given by

$$\mathbf{M}_{UU}\left(u^K, 0\right)\Delta u + R_U\left(u^K, 0, 0\right) = 0 . \qquad (50)$$

485

486   (2) The extended Blatter-Pattyn approximation from §3.4.2 becomes

487

$$R(u,w,p) = \begin{bmatrix} \mathcal{M}_U(u,0) + \mathbf{M}_{UP}p + F_U \\ \mathbf{M}_{WP}p \\ \mathbf{M}_{UP}^T u + \mathbf{M}_{WP}^T w \end{bmatrix} = 0 , \tag{51}$$

488   with the Newton-Raphson iteration given by

489

$$\mathbf{M}(u^K)\Delta U^{K+1} + R(u^K, w^K, p^K) = 0 , \tag{52}$$

490   where the Hessian matrix is

491

$$\mathbf{M}(u) = \begin{bmatrix} \mathbf{M}_{UU}(u,0) & 0 & \mathbf{M}_{UP} \\ 0 & 0 & \mathbf{M}_{WP} \\ \mathbf{M}_{UP}^T & \mathbf{M}_{WP}^T & 0 \end{bmatrix} . \tag{53}$$

492

493   **4.3 Discrete Solvability Issues**

494   **4.3.1 Solvability of the Stokes and Blatter-Pattyn Models**

495

496   Consider the solution of the three linear matrix problems (47), (50), (52) associated with

497   the Newton-Raphson solution of the Stokes and the Blatter-Pattyn approximate models.

498   While there are no issues in the continuous case, this is not so in the discrete case as

499   noted earlier. The discrete system to be solved has the general form

500

$$\mathbf{M}\left\{ \begin{array}{c} \mathbf{u} \\ p \end{array} \right\} = \begin{bmatrix} \mathbf{A} & \mathbf{B}^T \\ \mathbf{B} & 0 \end{bmatrix} \left\{ \begin{array}{c} \mathbf{u} \\ p \end{array} \right\} = \left\{ \begin{array}{c} \mathbf{f} \\ g \end{array} \right\} , \tag{54}$$

501   where $\mathbf{A}$ is a symmetric, positive definite, invertible matrix, and the variables $\mathbf{u}, p$ refer

502   to the Newton-Raphson variable increments. The form (54) is characteristic of Stokes-

503   type problems, or more generally of constrained minimization problems using Lagrange

504   multipliers. In finite element terminology these are referred to as mixed problems,

505   meaning that velocity components and the pressure occupy different finite element

506   spaces, or saddle point problems, meaning that the solution of (54) is at a saddle point

507   with respect to the velocity and pressure variables of the quadratic form associated with

508   (54). The matrix $\mathbf{M}$ is symmetric but indefinite, with $n_u + n_w$ positive and n_p negative

509   eigenvalues. Discretizations of this type may lack stability in the sense that convergence

510   to the saddle point cannot be achieved (Auricchio et al., 2017). The common way to

511   resolve this issue is to require the use of finite elements that satisfy the Ladyzhenskaya–

512 Babuška–Brezzi (LBB, or inf-sup) condition on matrix $\mathbf{B}^T$ in (54). There is a very large

513 literature on the subject, e.g., Boffi et al. (2008), Elman et al. (2014), Auricchio et al.

514 (2017). Testing for stability is not trivial. However, collections of inf-sup stable

515 elements for the Stokes equations may be found in many papers and books on mixed

516 methods, e.g., Boffi et al. (2008). The popular second-order Taylor-Hood P2-P1 element

517 (Hood and Taylor, 1973) is an example of an inf-sup stable element. Some results using

518 this element are shown in Fig. 13 for Test B, one of the test problems described in

519 Appendix C.

520

521   The two Blatter-Pattyn versions do not fall into this general category. The

522 standard Blatter-Pattyn model, (49)-(50), excludes matrices $\mathbf{B}, \mathbf{B}^T$ and solves only the

523 positive-definite matrix $\mathbf{A}$, making it a well-behaved unconstrained minimization

524 problem. The extended Blatter-Pattyn model, (51)-(52), experiences a different problem.

525 It is characterized by a decoupled equation for the pressure that involves the matrix $\mathbf{M}_{WP}$,

526 which is usually not square and therefore not invertible. Solution for the discrete

527 pressure is only possible when this matrix is invertible, which at minimum requires a

528 square matrix, i.e., $n_p = n_w$, and this depends on the finite element mesh chosen for the

529 discretization. For example, the Taylor-Hood (P2-P1) element mentioned previously

530 cannot be used because it typically has $n_p \ll n_w$ and therefore the linear system is

531 overdetermined for the pressure and underdetermined for the horizontal velocity w.

532

533   In the following section we introduce an alternative method for obtaining well-

534 posed formulations of all these models, including the extended Blatter-Pattyn model

535 discussed above, by the use of meshes that permit inverting the continuity equation for

536 the vertical velocity in terms of the horizontal velocity components.

537

538 **4.3.2 A Special Case: Invertible Continuity Equation**

539

540 In the continuous case, the Blatter-Pattyn approximation (§3.4) implies that vertical

541 velocity w is obtainable from the continuity equation after having solved for the

542 horizontal velocities u, v. This is always possible in the continuum but may not be so in

543 the discrete case, as noted in the extended Blatter-Pattyn approximation. Continuing with

544 the 2D case from §4.1 for simplicity, the discrete continuity equation from (46) or (51) is

545 given by

546
$$\mathbf{M}_{UP}^{T}u + \mathbf{M}_{WP}^{T}w = 0 \ . \tag{55}$$

547 For this to be solvable for w in terms of the horizontal velocity requires that matrix $\mathbf{M}_{WP}^{T}$

548 be invertible, i.e., it must be square and full rank. With an invertible matrix, solving (55)

549 we obtain

550
$$w(u) = -\mathbf{M}_{WP}^{-T}\mathbf{M}_{UP}^{T}u \ , \tag{56}$$

551 where $\mathbf{M}_{WP}^{-T}$ is the inverse of $\mathbf{M}_{WP}^{T}$. Note that

552
$$\mathbf{M}_{WP}^{-T} = \left(\mathbf{M}_{WP}^{T}\right)^{-1} = \left(\mathbf{M}_{WP}^{-1}\right)^{T} \tag{57}$$

553 since, if matrix $\mathbf{M}_{WP}^{T}$ is invertible then so is its transpose $\mathbf{M}_{WP}$. In general $\mathbf{M}_{WP}^{T}$ is an

554 $n_p \times n_w$ matrix so, at minimum, for solvability we require that

555
$$n_p = n_w \ . \tag{58}$$

556 If Lagrange multipliers are to be used, the number of unknown pressures n_p must be

557 augmented by the number of Lagrange multipliers and therefore (58) would become

558 $n_p + n_{\lambda_z} + n_{\Lambda} = n_w$ (See Appendix A, §A2, for more details). Assuming that we are

559 dealing with reasonable discretizations, we shall presume that $\mathbf{M}_{WP}^{T}$ is full rank. In the

560 following, we therefore refer to (58) (or more correctly, to the invertibility of $\mathbf{M}_{WP}^{T}$) as

561 the solvability condition. In Appendix A we present several meshes and elements that

562 satisfy this condition, including the P1-E0 element used in most of the 2D test problems

563 in this paper.

564

565   Invertibility of the continuity equation has several important implications. We

566 noticed earlier that the extended Blatter-Pattyn model does not work with a Taylor-Hood

567 P2-P1 mesh where the solvability condition is not satisfied. However, using a variant of

568 the Taylor-Hood mesh that does satisfy the solvability condition, the P2-E1 mesh

569 illustrated in Fig. 13A, allows this model to work well. Additionally, we find that the

570 solvability condition is a prerequisite for the new Stokes approximations discussed in

571 §6.2.

572

573   The solvability condition can also be used to convert the Stokes variational

574 principle, (15) or (32), from a constrained to an unconstrained minimization problem.

575 Consider the discrete form of the functional given by (45). Using a mesh that satisfies

576   the solvability condition, and assuming that the vertical velocity $w(u)$ from (56) is

577   available, one may substitute it into functional (45). The term involving pressure drops

578   out because continuity is satisfied, and one obtains a functional in terms of horizontal

579   velocity u only,

580
$$\mathcal{A}(u) = \mathcal{M}(u, w(u)) + u^T F_U + w(u)^T F_W . \qquad (59)$$

581   This now represents an unconstrained minimization problem since the functional

582    $\mathcal{M}(u, w(u))$ is positive semi-definite. Taking the variation with respect to the horizontal

583   velocity variables u, as in §4.1, one obtains the discrete Euler-Lagrange system of

584   equations for finding the minimum,

585
$$\mathcal{M}_U(u, w(u)) - \mathbf{M}_{UP} \mathbf{M}_{WP}^{-1} \mathcal{M}_W(u, w(u)) + (F_U - \mathbf{M}_{UP} \mathbf{M}_{WP}^{-1} F_W) = 0 . \qquad (60)$$

586   This is a set of n_u nonlinear equations for the discrete horizontal velocity variables u that

587   is analogous to the standard Blatter-Pattyn problem of §3.4.1, except that here it

588   represents the full Stokes problem. As in the Blatter-Pattyn case, the solution is expected

589   be well behaved and stable. However, the Newton-Raphson iterative solution of (60)

590   involves a dense Hessian matrix that makes the solution very costly and impractical for

591   large problems.

592

593   Perhaps the main reason for the importance of the solvability condition is that it

594   can function as an alternative for the inf-sup condition to ensure solution stability. As

595   explained in Appendix B, solution stability of the saddle point problem (54) is

596   compromised if the matrix $\mathbf{B}^T$ has a non-empty null space, which in turn is related to the

597   pressure solution containing spurious modes. On the other hand, use of a mesh that

598   satisfies the solvability condition produces a matrix equation for the pressure that is

599   invertible. This means that the corresponding Stokes saddle point problem is well posed

600   when solved on a mesh that satisfies the solvability condition, without the need to satisfy

601   the inf-sup condition.

602

603   **5. Comparison of the Standard and Transformed Stokes Models**

604

605   The standard and transformed Stokes models are expected to converge to the same

606   solution. To verify this we do a number of calculations for some 2D test problems based

607   on the ISMIP-HOM benchmark (Pattyn et al, 2008). These tests, Tests B and D*are

608   described in Appendix C. Test B features no-slip boundary conditions on a sinusoidal

June 27, 2025

609   bed, and Test D* evaluates sliding of the ice sheet along a flat bed in the presence of

610   sinusoidal friction. The tests are discretized using P1-E0 elements on a regular mesh

611   composed of n quadrilaterals in the x-direction and m quadrilaterals in the z-direction,

612   illustrated in Fig. A1, with each quadrilateral divided into two triangles. Results are

613   presented for two domain lengths, $L = 5$ km and 10 km, to test the aspect ratio range

614   where the Blatter-Pattyn model begins to fail. A relatively coarse mesh, i.e., $m = n = 40$,

615   is used, except when we look at convergence with mesh refinement in Fig. 3.
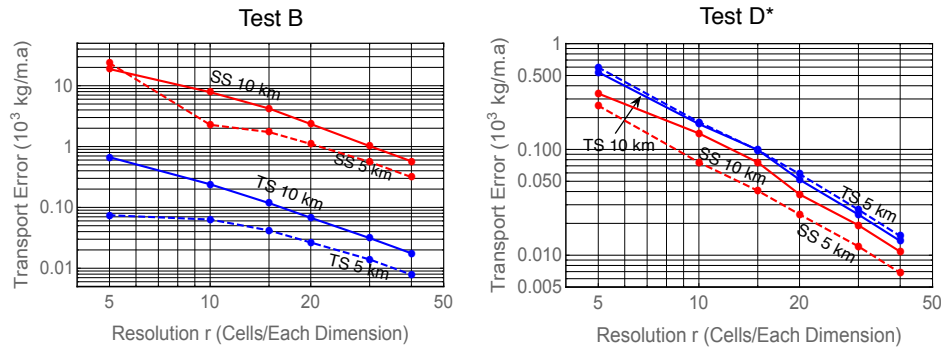
617   **Figure 3.** Convergence of ice transport in Tests B and D* with mesh refinement.

618   Transformed Stokes (TS) plots are in blue and standard Stokes plots (SS) are in red.

619
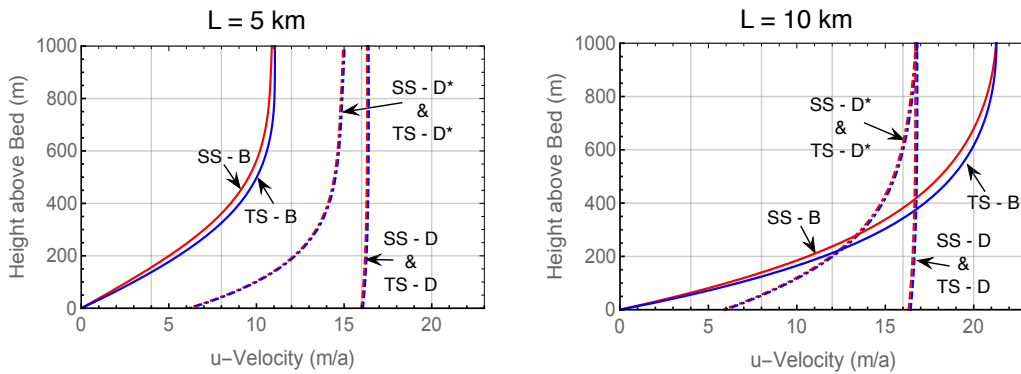
621   **Figure 4.** The u-velocity profile at location $x = L$ as a function of height from the bed.

622

623   Fig. 3 evaluates the convergence of the two Stokes formulations as a function of

624   mesh resolution r, where r is the number of quadrilaterals in either direction. The

625   models converge to the same value of the transport, obtained by Richardson

626   extrapolation, and convergence is second order as expected from the use of linear

627   elements. Interestingly, in Test B the transformed Stokes model is considerably more

628   accurate at all resolutions than the standard model. As a result, the standard Stokes

629   calculations are not fully converged even at the 40x40 resolution. Fig. 4 shows the

630   vertical profiles of the horizontal velocity u at outflow, $x = L$. Results from the no-slip

631   Test B problem and the two frictional sliding problems, Tests D and D*, are plotted. The
632   Test D profile from the ISMIP-HOM benchmark is almost vertically constant, indicating
633   that the value for basal friction that was originally chosen is too small. This motivated
634   the change of Test D to Test D* in Appendix C, with larger basal friction.

635
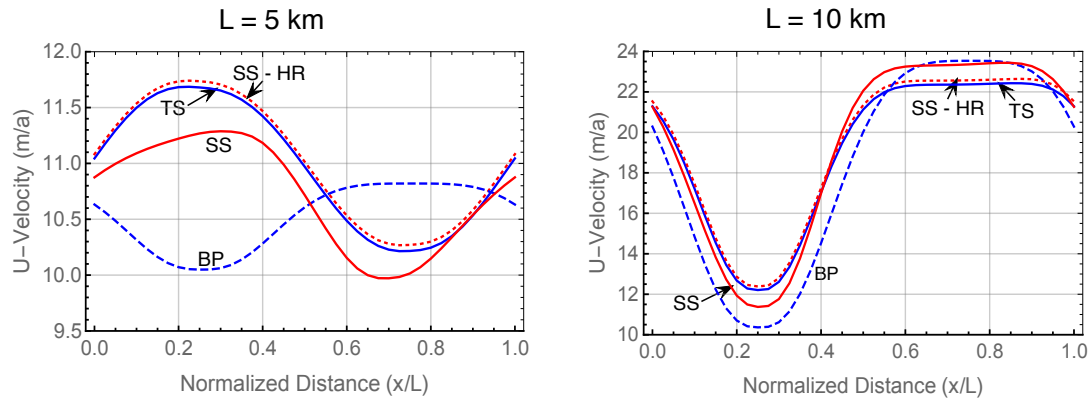
636   **Figure 5.** Upper surface u-velocity, $u(x,z_s)$ - Test B, No-slip boundary conditions.

637

638
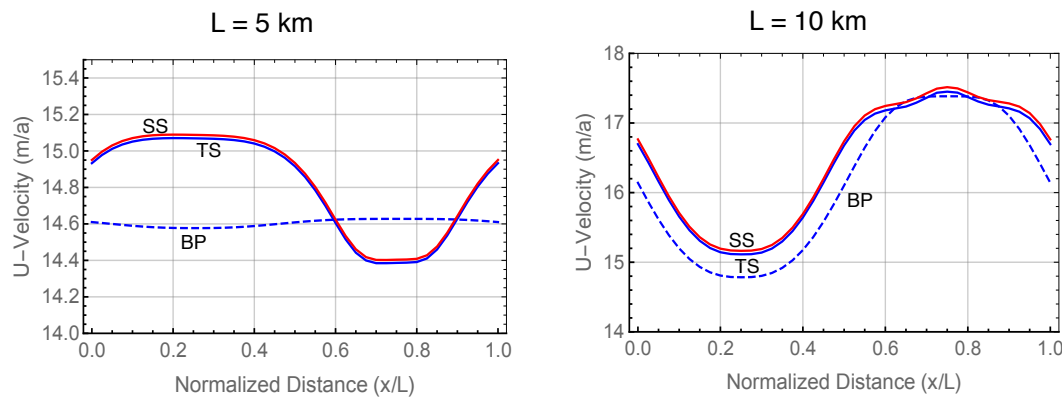
639   **Figure 6.** Upper surface u-velocity, $u(x,z_s)$ - Test D*, Modified frictional sliding.

640

641   Figs. 5 and 6 show the u-velocity at the ice sheet upper surface for Tests B and
642   D*. This is the benchmark used in ISMIP-HOM to compare different ice sheet models.
643   Four cases are compared: the standard Stokes model (SS), the transformed Stokes model
644   (TS), the Blatter-Pattyn (BP) model, and for reference, a very high resolution full-Stokes
645   Test B calculation "oga1" (SS-HR) from the ISMIP-HOM paper and also Gagliardini and
646   Zwinger (2008). The TS and the SS-HR plots lie on top of one another (they have been
647   offset slightly for clarity), indicating that the TS model is already fully converged. As
648   before, the SS model is not yet converged in Test B, particularly at $L = 5$ km. As in the
649   ISMIP-HOM study, the Blatter-Pattyn calculation (BP) shows large deviations from the

650   Stokes results, especially so at $L = 5$ km where the surface velocity is entirely out of

651   phase with the Stokes results. Fig. 6 shows that results for the SS and TS models

652   essentially coincide in Test D* (the SS plot has been slightly offset upward for clarity).

653   As expected, Blatter-Pattyn results show noticeable error at $L = 10$ km and very large

654   error at $L = 5$ km. Pressure results are not presented since they have no physical

655   significance. However, it may be noted that pressures on the P1-E0 mesh are particularly

656   smooth and well behaved.

657

658   **6. Applications of the Transformed Stokes Model**

659   **6.1 Adaptive Switching between Stokes and Blatter-Pattyn Models**

660

661   A way of reducing the cost of a full Stokes calculation is to use it adaptively together

662   with a cheaper approximate model. That is, one may use the cheaper model in those parts

663   of a problem where it is accurate, and the more expensive full Stokes model where the

664   approximate model loses accuracy. An example of such an adaptive approach is the

665   tiling method by Seroussi et al. (2012). However, such methods have drawbacks such as

666   the need to incorporate two or more presumably quite different models into a single

667   model together with a transition zone to couple the disparate models.

668

669   On the other hand, the use of the transformed Stokes model is particularly simple

670   in such an adaptive role because it may be locally switched between the Stokes and

671   Blatter-Pattyn cases by switching the parameter $\xi \in \{0,1\}$ on and off. Either the standard

672   or the extended Blatter-Pattyn models may be used. Use of the standard Blatter-Pattyn

673   approximation ($\xi, \hat{\xi} = 0$) would be somewhat cheaper but it would require more

674   complicated programming, i.e., it would need coupling to the Stokes model with $p = 0$

675   and $w = w(u,v)$ at the interface between models. Use of the extended Blatter-Pattyn

676   approximation ($\xi = 0, \hat{\xi} = 1$) would be much simpler since then both the Stokes and

677   Blatter-Pattyn parts of the code will then have the same number of degrees of freedom.

678   However, as explained in §4.3, the extended Blatter-Pattyn model requires a mesh

679   satisfying the solvability condition such as the P1-E0 mesh. Although a little more

680   expensive than standard Blatter-Pattyn, the extended Blatter-Pattyn model is still much

681   cheaper than the full Stokes model. For example, the extended Blatter-Pattyn calculation

682   of Test B at a 40x40 resolution, as in Figs. 5 and 6, is some 4.3 times cheaper than the

683   corresponding transformed Stokes calculation.

June 27, 2025

684

685   To demonstrate adaptive switching with a transformed Stokes model, we

686 introduce a new problem, Test O, described in Appendix C and illustrated in Fig. C1.

687 This consists of an inclined ice slab whose movement is obstructed by a thin obstacle

688 protruding 20% of the ice depth up from the bed. No-slip boundary conditions are

689 applied along the bed and the obstacle. Because of the localized nature of the obstacle,

690 the condition for the validity of the Blatter-Pattyn approximation, namely (37), must fail

691 near the obstacle and therefore the full Stokes model is needed for good accuracy, at least

692 locally.

693
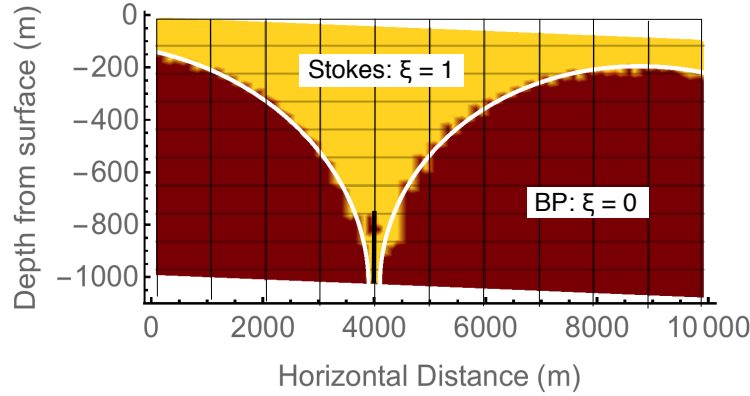
694 **Figure 7.** Mask function (white curve, $z = F_M(x)$) to indicate where the Stokes and BP

695 models are activated in the 20% obstacle test problem. The dark brown region delineates

696   the region where $\left|\partial w/\partial x\right| \leq 0.1\left|\partial u/\partial z\right|$ from a Blatter-Pattyn calculation.

697

698   To implement the method, we first use a Blatter-Pattyn calculation to determine

699 regions where $\left|\partial w/\partial x\right| \leq 0.1\left|\partial u/\partial z\right|$, approximately localizing where the Blatter-Pattyn

700 approximation is valid. This determines a mask function $z = F_M(x)$, illustrated in Fig. 7

701 by the white curve, specifying where the two models must be used. Defining the centroid

702 of a triangular element by (x_C, z_C), the code makes a selection in each element:

703
$$z_C \leq F_M(x_C) \quad \Rightarrow \quad \text{Set } \xi = 0, \quad \text{i.e., the Blatter-Pattyn region,}$$
$$z_C > F_M(x_C) \quad \Rightarrow \quad \text{Set } \xi = 1, \quad \text{i.e., the Stokes region.}$$

704 The Stokes region occupies the upper part of the domain in Fig. 7 and includes the

705 obstacle, while the Blatter-Pattyn region occupies much of the bottom part of the domain.

706 A transition zone, e.g., $0 \leq \xi(x, z) \leq 1$, could be implemented but this was not done in the

707 present case.

June 27, 2025

708

709   Results from the adaptive-hybrid calculation are shown in Fig. 8, showing curves

710   of the horizontal velocity u at seven different vertical locations specified as a percentage

711   of the distance between top and bottom, with $\sigma = 100\%$ at the top surface. The top right

712   panel shows the results for the adaptive-hybrid calculation (AH), and the top left panel

713   and bottom panel show results for the Stokes (TS) and Blatter-Pattyn (BP) calculations,

714   respectively. All calculations use the 40x40 mesh resolution. The adaptive-hybrid

715   results are very similar to the full Stokes results, reproducing most features of the

716   velocity profiles, including the velocity bump at the top surface, indicating that even the

717   top surface feels the presence of the obstacle. The Blatter-Pattyn results are much less

718   accurate, completely missing the details of the flow near the obstacle. The calculated

719   RMS error relative to the Stokes results in the Blatter-Pattyn case is 0.493 m/a and 0.440

720   m/a in the adaptive-hybrid case. It is larger in the Blatter-Pattyn case, as expected, but

721   the difference is less than expected from the visual differences in Fig. 8. Nonetheless, the

722   adaptive-hybrid method is successful even if judged by the Fig. 8 results alone.

723   However, the present calculations are proof of concept only and not representative of

724   practical computational methods so computational cost comparisons would not be

725   meaningful.

726
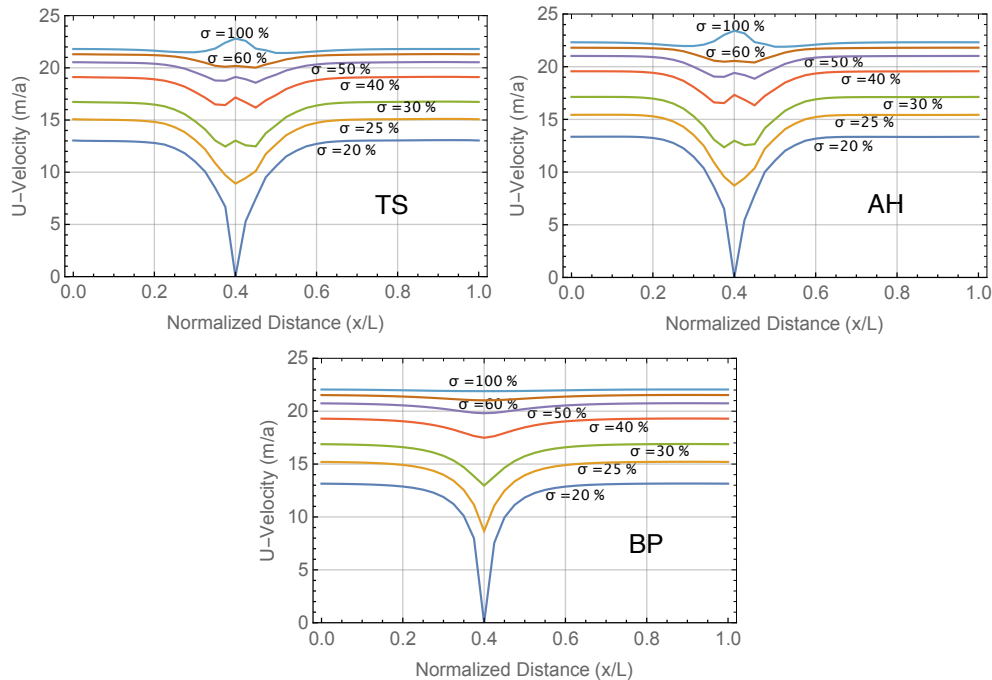
727   **Figure 8.** Horizontal velocity profiles for the Transformed Stokes (TS),

728   the Adaptive-Hybrid (AH), and the Blatter-Pattyn (BP) models in Test O.

729

June 27, 2025

730 **6.2. Two New Stokes Approximations**

731

732 As shown in §3.4, simply setting $w = 0$ in the second invariant $\tilde{\dot{\varepsilon}}^2$ in the transformed

733 functional $\tilde{\mathcal{A}}$ results in the standard Blatter-Pattyn approximation. This suggests that

734 approximating rather than neglecting the vertical velocity w in the functional would

735 create better approximations. We will look at two such methods, although others may be

736 possible. The first method, called the Herterich approximation, may be understood as

737 Picard iteration of the transformed functional (32) where the vertical velocity, obtained

738 from the solution of the continuity equation, is a lagged value from the previous iteration.

739 Two ways of implementing this method are described. The second method, to be called

740 the Dual-Mesh approximation, approximates the vertical velocity by discretizing the

741 continuity equation on a coarser mesh. Since vertical velocity is obtained from inverting

742 the continuity equation, this has the effect of approximating the vertical velocity and

743 reducing the number of pressure and vertical velocity variables while preserving the

744 structure of the Stokes model. The degree of approximation is determined by the amount

745 of coarsening of the continuity mesh.

746

747 **6.2.1 The Herterich Approximation**

748

749 Noting that $\tilde{P} = 0$ in the Blatter-Pattyn approximation, we drop the term involving

750 pressure from the transformed functional (32) in the 2D case to obtain a new pressure-

751 free functional,

752
$$\tilde{\mathcal{A}}_{PS1}[u] = \int_V dV \left[\frac{4n}{n+1} \eta_0 \left(\tilde{\dot{\varepsilon}}^2 \right)^{(1+n)/2n} + \rho g u \frac{\partial z_s}{\partial x} \right] + \frac{1}{2} \int_{S_{B2}} dS \, \beta(x) \left(u^2 + \zeta \left(u \, n_x / n_z \right)^2 \right), \quad (61)$$

753 where

754
$$\tilde{\dot{\varepsilon}}^2 = \left(\frac{\partial u}{\partial x} \right)^2 + \frac{1}{4} \left(\frac{\partial u}{\partial z} + \frac{\partial w}{\partial x} \right)^2 \qquad (62)$$

755 is the 2D version of the transformed second invariant, (27). Incompressibility is

756 incorporated separately by the use of a second functional,

757
$$\tilde{\mathcal{A}}_{PS2}[p] = \int_V dV \, p \left(\frac{\partial u}{\partial x} + \frac{\partial w}{\partial z} \right). \qquad (63)$$

758 Both functionals make use of direct substitution for boundary conditions, as in (15) and

759 (32). Note that functional (61) involves both velocity components u, w but the variation

760 is to be taken only with respect to u. Similarly, functional (63) involves u, w, p but

June 27, 2025

761 variation is taken only with respect to p. Here we are effectively viewing the pressure

762 p as a "test function" in the finite element sense. This gives some additional flexibility

763 to create elements that satisfy the solvability condition (58). For example, in a

764 triangulation some pressures may be assigned to every two triangles, as in a P1-E0 mesh,

765 while others may be assigned to a single triangle so as to achieve an equal number of

766 pressure and vertical velocity variables.

767

768 The variation of $\tilde{\mathcal{A}}_{PS1}[u]$ with respect to u results in a set of n_u discrete Euler-

769 Lagrange equations corresponding to the u-momentum equation,

$$\hat{R}_U(u,w) = \frac{\partial \tilde{\mathcal{A}}_{PS1}(u,w)}{\partial u} = \mathbf{M}_U(u,w) + F_U = 0 . \tag{64}$$

771 When w is set to zero, this is just the Blatter-Pattyn model, (49). The discrete variation

772 of $\tilde{\mathcal{A}}_{PS2}[p]$ with respect to p, results in the n_p equations of the discrete continuity

773 equation (55),

$$\hat{R}_P(u,w) = \frac{\partial \tilde{\mathcal{A}}_{PS2}(u,w,p)}{\partial p} = \mathbf{M}_{UP}^T u + \mathbf{M}_{WP}^T w = 0 . \tag{65}$$

775 These two systems are combined to form the discrete equations of the Herterich

776 approximation,

$$\hat{R}(u,w) = \left[\hat{R}_U(u,w), \hat{R}_P(u,w) \right]^T = 0 . \tag{66}$$

778 This is a system of $n_u + n_p$ equations to determine the $n_u + n_w$ discrete variables u, w,

779 implying that (66) is only a viable system for u, w on meshes satisfying the solvability

780 condition, $n_p = n_w$. Just as in the standard Blatter-Pattyn approximation in §3.4.1, the

781 vertical momentum equation is missing, but instead of neglecting w here the vertical

782 velocity is obtained consistently from the continuity equation.

783

784 The continuum form of the discrete Euler-Lagrange system (64), (65) is given by

$$\frac{\partial}{\partial x}\left(4\tilde{\mu}\frac{\partial u}{\partial x} \right) + \frac{\partial}{\partial z}\left(\tilde{\mu}\left(\frac{\partial u}{\partial z} + \frac{\partial w}{\partial x} \right) \right) - \rho g \frac{\partial z_s}{\partial x} = 0, \qquad \frac{\partial u}{\partial x} + \frac{\partial w}{\partial z} = 0, \tag{67}$$

786 together with the boundary conditions,

$$4\tilde{\mu}\frac{\partial u}{\partial x}n_x + \tilde{\mu}\left(\frac{\partial u}{\partial z}+\frac{\partial w}{\partial x}\right)n_z = 0 \ \text{ on } \ S_S, \quad u=w=0 \ \text{ on } \ S_{B1},$$

$$4\tilde{\mu}\frac{\partial u}{\partial x}n_x + \tilde{\mu}\left(\frac{\partial u}{\partial z}+\frac{\partial w}{\partial x}\right)n_z + \beta(x)\left(u+\zeta\,u\left(n_x/n_z\right)^2\right)=0, \ \ w=-u\,n_x/n_z, \Bigg\} \ \text{ on } \ S_{B2},$$

787 (68)

788   where the viscosity is $\tilde{\mu}=\eta_0\left(\tilde{\varepsilon}^2\right)^{(1-n)/2n}$ as in (26). Remarkably, these are the same

789   equations used by Herterich (1987) in a model to study the transition zone between an ice

790   sheet and an ice shelf[1]. As a result, this approximation is named the Herterich model.

791   The Herterich model predates the widely used Blatter-Pattyn model by some eight years

792   but, in contrast to Blatter-Pattyn, it has fallen into obscurity.

793

794   There are two algorithms for solving the Herterich system (66), as follows

795   (1) Newton/Picard iteration version:

796   If we lag the vertical velocity, i.e., $w^{K+1}=w^K \Rightarrow \Delta w=0$ in the first equation of (70), we

797   obtain a Picard iteration algorithm, as follows

$$\text{Starting from } K=0, \ choose \text{ an initial guess, } u^0 \neq 0, w(u^0),$$
$$\text{Solve: } \mathbf{M}_{UU}\left(u^K,w^K\right)\Delta u + \hat{R}_U\left(u^K,w^K\right)=0,$$
$$u^{K+1}=u^K+\Delta u, \quad w^{K+1}=w\left(u^{K+1}\right)=-\mathbf{M}_{WP}^{-T}\mathbf{M}_{UP}^T u^{K+1},$$
$$K=K+1, \qquad \text{Repeat until convergence.}$$

798 (69)

799   Each step of the iteration is inexpensive since it is equivalent to a step of the standard

800   Blatter-Pattyn model, (35). However, Picard iterations typically converge only linearly.

801   It remains to be seen which version is preferable in practice.

802   (2) Quasi-variational, Newton iteration version:

803   To obtain second order convergence we treat (66) as a single multidimensional nonlinear

804   system and solve it using Newton-Raphson iteration, as follows

$$\mathbf{M}_{UU}\left(u^K,w^K\right)\Delta u + \mathbf{M}_{UW}\left(u^K,w^K\right)\Delta w + \hat{R}_U\left(u^K,w^K\right)=0,$$
$$\mathbf{M}_{UP}^T u^{K+1}+\mathbf{M}_{WP}^T w^{K+1}=0.$$

805 (70)

806   where K is the iteration index and $\Delta u, \Delta w$ are defined previously, and $\mathbf{M}_{UU}(u,w)$ and

807    $\mathbf{M}_{UW}(u,w)$ are the same matrices as appear in (48). Convergence is rapid (quadratic)

808   once in the basin of attraction but each step is more expensive than in the Picard iteration

---

[1] Reference provided by C. Schoof.

June 27, 2025

809   version. Both versions depend on an invertible continuity equation to obtain $w = w(u)$.

810   However, good approximations of the vertical velocity $w(u)$ may already be available in

811   existing codes; for instance, in MALI (Hoffman et al., 2018), a code based on the Blatter-

812   Pattyn approximation, to obtain the vertical velocity w for the advection of ice

813   temperature (Mauro Perego, private communication).

814
815
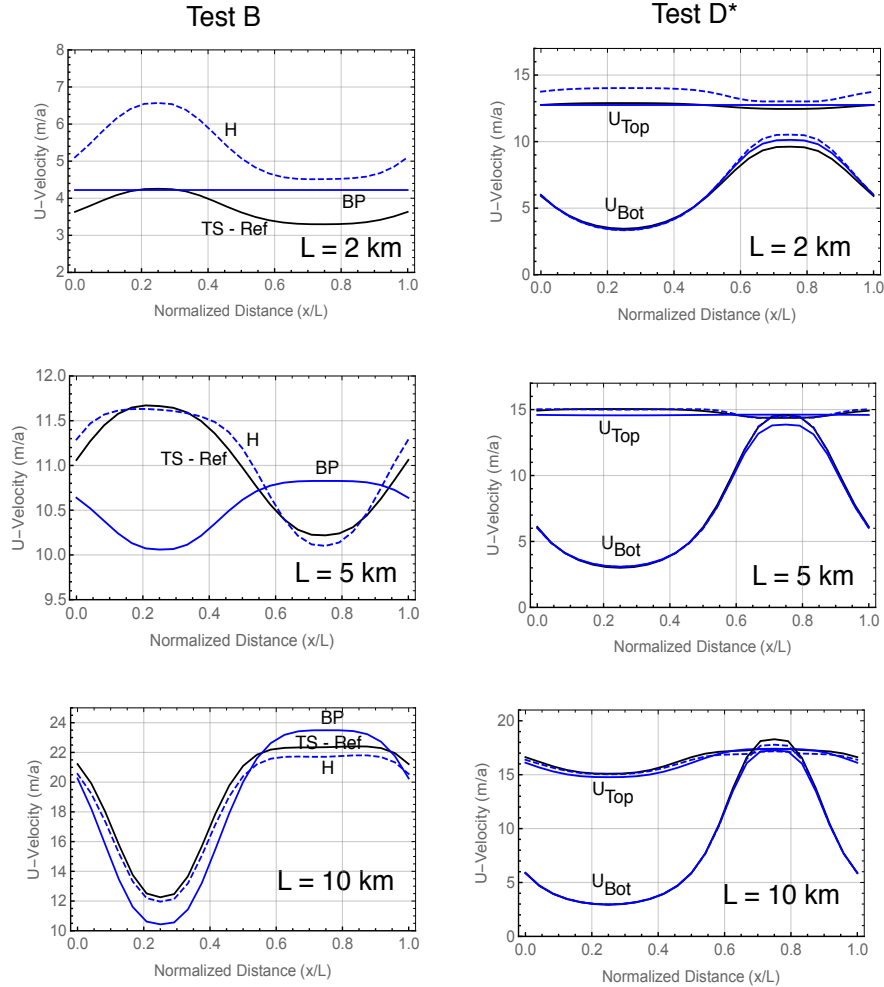
816   **Figure 9.** Comparing Approximations. Test B, Upper surface u-velocity,

817   and Test D*, Upper and Lower surface u-velocity.

818   TS-Ref: Transformed Stokes; BP: Blatter-Pattyn; H: Herterich.

819   Resolution: 24x24.

820

821   Both Herterich algorithms converge to the same result. Fig. 9 compares the

822   Herterich (H) and the Blatter-Pattyn (BP) approximations to a reference exact

823   transformed Stokes solution (TS-Ref) for Test B results on the left and Test D* results on

June 27, 2025

824   the right at three problem aspect ratios in the range where small aspect ratio

825   approximation begin to fail, $\varepsilon = H_0 / L = 0.1, 0.2, 0.5$, where $H_0 = 1000\,m$ is the nominal

826   ice thickness and L is the domain length. The Herterich approximation might be

827   expected to be more accurate than the BP approximation since it retains more terms from

828   the transformed Stokes model equations but this is not borne out in the Fig. 9. The

829   Herterich approximation is indeed more accurate in Test B at $L = 5, 10\,km$. This is

830   confirmed by the RMS u-Error results in Fig. 12 where the Herterich model is two to

831   three times more accurate than BP. However, the opposite is the case at $L = 2\,km$ in both

832   Tests B and D*, although the results in Test B may be deceptive because only the upper

833   surface velocity is displayed (lower surface velocity is zero) and this expands the scale

834   accentuating differences between the three cases. Test D* results are closely clustered

835   except in the $L = 2\,km$ case where, surprisingly, the Herterich approximation is the least

836   accurate. These results suggest that the Herterich approximation may need to be

837   evaluated further.

838

839   **6.2.2 A "Dual-Mesh" Transformed Stokes Approximation**

840

841   In the Herterich approximation we approximated the vertical velocity directly in the

842   second invariant as it appeared in the variational functional. Here we approximate w

843   indirectly by instead approximating the continuity equation that is then used to determine

844   the vertical velocity. That is, the continuity equation is discretized on a mesh coarser

845   than the one used for the momentum equations. The vertical velocity on the coarser mesh

846   is then interpolated to appropriate locations on the finer mesh. This reduces the number

847   of unknown variables in the problem, making it cheaper to solve but hopefully without

848   serious loss of accuracy. As described in Appendix C, our test problem meshes are

849   logically rectangular, i.e., divided into n cells horizontally and m cells vertically. The

850   coarse mesh is constructed by dividing the fine mesh into s equal segments in each

851   direction. This assumes that the integers n and m are each divisible by s, so that there

852   are nm/s^2 coarse cells in total with each coarse cell containing s^2 fine cells. The

853   primary mesh (i.e., the fine mesh) is chosen to have $n = m = 24$, i.e., a reference 24×24

854   fine mesh, so as to maximize the number of different coarse meshes available. Coarse

855   meshes are constructed using $s = 2, 3, 4, 6$, and this resulted in fine/coarse mesh

856   combinations labeled by $24 \times 12, 24 \times 8, 24 \times 6, 24 \times 4$, respectively. Similar to a P1-E0

857   fine mesh, coarse mesh vertical velocities w are located at vertices and pressures at

858 vertical edges. Fig. 10 illustrates the case of a single coarse cell and four fine

859 quadrilateral cells for a mesh fragment with $n=m=2$ and $s=1$. In Test B problems

860 with direct substitution for basal boundary conditions there will be nm u-variables and

861 nm/s^2 w- and p-variables each, for a total of $nm\left(1+2/s^2\right)$ unknown variables,

862 considerably fewer than the $3nm$ variables in the full resolution mesh. The coarse mesh

863 terms in the functional that are affected, $\tilde{P}\left(\partial u/\partial x+\partial w/\partial z\right)$ and $\partial w/\partial x$, are computed

864 by interpolating coarse mesh variables to the fine mesh. We consider two versions of the

865 approximation depending on how the coarse mesh terms are interpolated to the fine mesh.
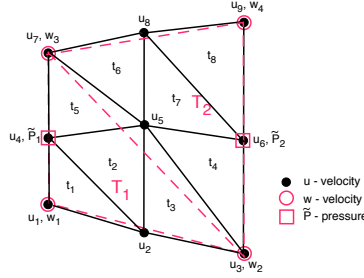
866
867
868 **Figure 10.** A Sample of a Coarse/Fine P1-E0 Mesh for the Dual-Mesh Approximation.

869 Resolution: $n=m=2, s=1$. Coarse mesh is in red, fine mesh in black.

870

871 (1) Approximation A, Bilinear interpolation:

872 Referring to Fig. 10, the four velocities at the vertices of the coarse mesh

873 quadrilateral, i.e., u_1,u_3,u_7,u_9 and w_1,w_2,w_3,w_4 , are used to obtain u,w at the remaining

874 five vertices of the fine mesh by means of bilinear interpolation. Thus, the five velocities

875 u_2,u_4,u_5,u_6,u_8 are obtained in terms of vertex velocities u_1,u_3,u_7,u_9 , and similarly for the

876 w velocities. The resulting complete set of fine mesh variables is used calculate the

877 divergence $D=\left(\partial u/\partial x+\partial w/\partial z\right)$ and the quantity $\partial w/\partial x$ in each of the eight triangular

878 elements $t_1,t_2,\cdots,t_8$ of the fine mesh. Coarse mesh pressures $\tilde{P}_1,\tilde{P}_2$ are associated with

879 the coarse mesh triangles T_1,T_2 . The products $\tilde{P}_1 D$ in elements t_1,t_2,t_3,t_5 and $\tilde{P}_2 D$ in

880 elements t_4,t_6,t_7,t_8 are then accumulated over the entire mesh to obtain the quantity

881 $\tilde{P}\left(\partial u/\partial x+\partial w/\partial z\right)$ for use in the transformed functional $\tilde{\mathcal{A}}$. Similarly, the quantity

882 $\partial w/\partial x$ is computed in the fine mesh elements from coarse mesh variables for use in the

883 second invariant $\tilde{\dot{\varepsilon}}^2$.

June 27, 2025

884   (2) Approximation B, Linear interpolation:

885   In this version, the three velocities at the vertices of the two coarse mesh triangles

886   T_1 and T_2, i.e., u_1, u_3, u_7 and w_1, w_2, w_3 in T_1, and u_7, u_3, u_9 and w_3, w_2, w_4 in T_2,

887   approximate the divergence $D = \left(\partial u / \partial x + \partial w / \partial z \right)$ and $\partial w / \partial x$ as constant values in the

888   two coarse triangles. The constant values $\tilde{P}_1 D$, $\tilde{P}_2 D$ are then accumulated over the

889   entire mesh. The constant value $\partial w / \partial x$ in each coarse triangle is then distributed to each

890   of the eight fine mesh elements $t_1, t_2, \cdots, t_8$, depending on whether the centroid of the fine

891   triangular element is in T_1 or T_2. As in the previous case, this is then used in the second

892   invariant $\tilde{\dot{\varepsilon}}^2$ in the transformed functional $\tilde{\mathcal{A}}$.

893

894   While the number and type of unknown variables is the same in the two versions,

895   they differ considerably in accuracy as seen in Figs. 11 and 12. Fig. 11 compares the

896   upper surface u-velocity in approximations A and B, for the five mesh combinations, to

897   the reference 24x24 fine mesh transformed Stokes (TS) calculation. The corresponding

898   Blatter-Pattyn result is shown in Fig. 9. Fig. 12 summarizes and compares the overall

899   accuracy of all approximations by means of the RMS u-Error relative to the TS

900   calculation. As might be expected, the accuracy of Approx. A is better than Approx. B,

901   particularly in the case $L = 10$ km. Both dual-mesh versions are more accurate than the

902   BP and H approximations, except for the lowest 24x4 resolution of Approx. B. However,

903   it is surprising that the SS calculation is the least accurate but this is because SS is not yet

904   fully converged at this resolution (see Fig. 5).

905

906   A comparison of computational time relative to the TS calculation is presented in

907   Fig. 12 for the 24x24 resolution case. The cost of the BP approximation is substantially

908   lower than the cost of full Stokes, while the cost of the Herterich approximation is only

909   slightly higher than BP. This comparison is only qualitative because the present

910   calculations are not representative of the computer hardware or the methods used in

911   practical ice sheet modeling. Present calculations are proof of concept only, made on a

912   personal computer using the program Mathematica, a slow interpreted language. As a

913   result the cost comparisons are inaccurate and possibly misleading. No effort was made

914   to optimize the calculations or to take advantage of parallelization. Thus, for example,

915   the cost of dual-mesh approximations A and B is greatly affected by the cost of the

916   associated interpolations, making them more costly than even the unapproximated

917   calculations, TS and SS. However, the interpolations are highly parallelizable and would

918   contribute little to the cost in practical computations.

919
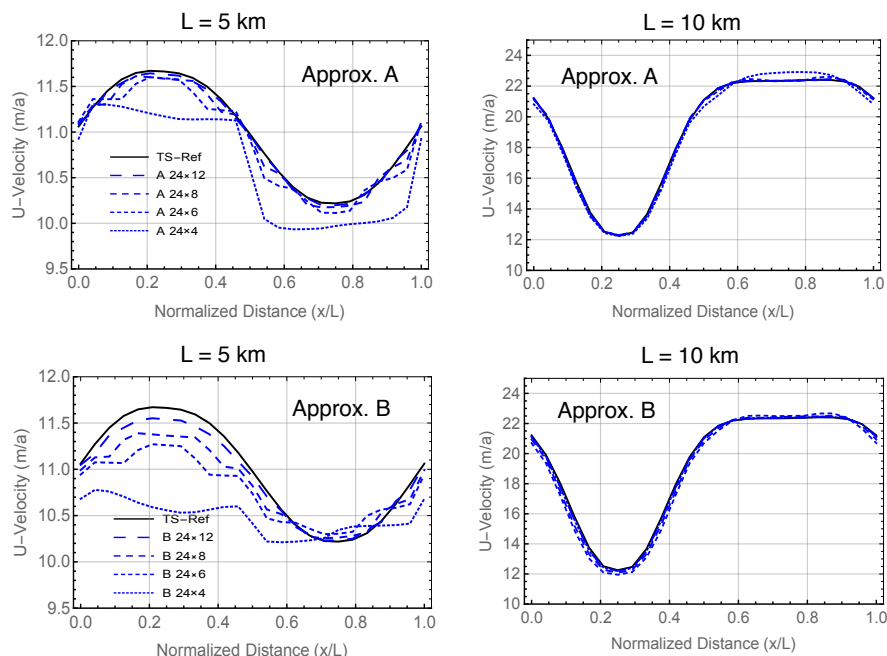
920   **Figure 11.** Comparing Approximations A and B. Test B. Upper surface u-velocity.

921   TS-Ref: Ref. Stokes (r x r = 24x24); Fine/Coarse resolutions (r x R = 24x12, 8, 6, 4).

922

923
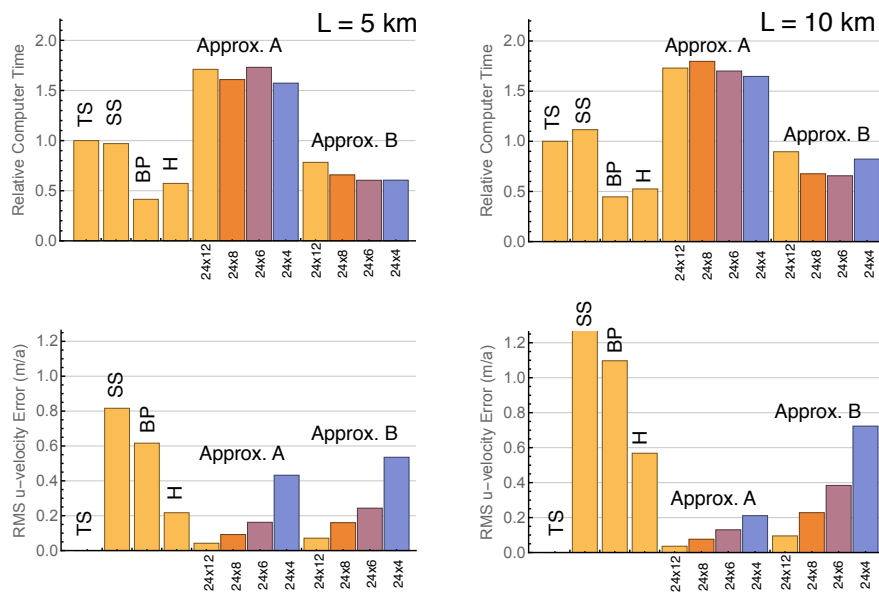
924   **Figure 12.** Comparing the Test B computer time and RMS u-Error results relative

925   to a TS calculation for Approximations BP, H, A, B, and the SS Stokes model.

926   TS, SS, BP, H: Resolution (r x r = 24x24); Approx. A, B: (r x R = 24x12, 8, 6, 4).

927

June 27, 2025

928 **7. Second-Order Discretizations**

929

930 So far we have used first-order elements, primarily P1-E0. However, in current practice

931 Stokes models are often based on second-order elements such as the popular Taylor-

932 Hood P2-P1 element (e.g., Leng et al., 2012; Gagliardini et al., 2013). In 2D the P2-P1

933 element, illustrated in Fig. 13A, has velocities on element vertices and edge midpoints

934 and pressures on element vertices, resulting in quadratic velocity and linear pressure

935 distributions. This element satisfies the inf-sup stability condition (e.g., Elman et al.,

936 2014) but does not satisfy the solvability condition (58) since $n_w \gg n_p$. For example, in

937 the present Test B calculations we have $n_w = 4nm$ and $n_p = n(m+1)$.

938
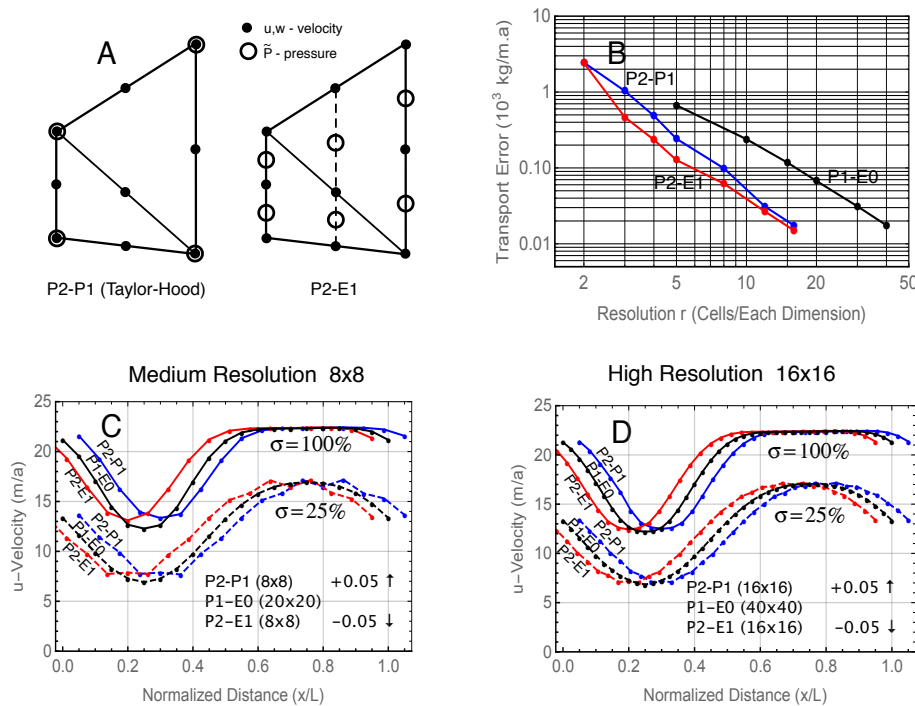
939 **Figure 13.** Comparing second-order discretizations based on the P2-P1 and P2-E1

940 elements from panel A to first-order discretizations using the P1-E0 element in Test B

941 calculations with L=10 km. Only transformed Stokes calculations are compared;

942 standard Stokes results behave similarly. Panel B compares the convergence and

943 accuracy of various schemes with increasing resolution, while panels C, D compare

944 horizontal velocities at medium and maximum resolutions.

945

946 Stokes models work well with a Taylor-Hood mesh as shown in Fig. 13 where

947 both the P2-P1 and P1-E0 models converge to a common solution. Recall that the P2-P1

948 mesh does not work with the extended Blatter-Pattyn approximation, a model that

949 requires the solvability condition. However, it is possible to construct a second-order

950 element consistent with an invertible continuity equation. This is the P2-E1 element, as

951 illustrated in Fig. 13A, which is second-order for velocities and linear for pressure, just

952 like the P2-P1 element, but the pressure is edge-based rather than vertex-based.

953 Pressures are located midway between velocities along vertical lines, as illustrated in Fig.

954 13A. As explained in Appendix A, this mesh must be constructed using vertical columns

955 of quadrilaterals. Since pressures are vertically collinear with velocities, as in the P1-E0

956 element, the analysis in Appendix A confirms that this element satisfies the solvability

957 condition (58). A 3D analog exists, as explained in Appendix A.

958

959   Fig. 13B shows the error in ice transport as a function of mesh refinement for the

960 second-order P2-P1 and P2-E1 meshes in transformed Stokes Test B calculations,

961 together with similar results for the first-order P1-E0 mesh from Fig. 3 for comparison.

962 Note that both second order models show approximately the same error at resolution

963 $r = 16$ as the first order P1-E0 model at resolution $r = 40$, and the same for coarser

964 resolutions such as $r = 8$ and $r = 20$, respectively. However, at a comparable resolution

965 or accuracy the second-order calculations are considerably more expensive than the first-

966 order calculations.

967

968   Panels C, D in Fig. 13 compare u-velocities from several Test B calculations

969 using the two second-order models to the first-order P1-E0 model results from Fig. 3.

970 Each panel shows upper surface velocities ($\sigma = 100\%$) in solid lines and velocities from

971 a surface a quarter of the way up from the bottom ($\sigma = 25\%$) in dashed lines. Panel C

972 shows medium resolution calculations ($r = 8, 20$ in the second-order and first-order

973 calculations, respectively) and panel D shows higher resolution calculations ($r = 16, 40$).

974 At these resolutions the accuracy of the first- and second-order calculations is very

975 similar so for clarity the second-order results are displaced horizontally from the first-

976 order results by 0.05 nondimensional units. The P2-E1 results in magenta are displaced

977 to the left and the P2-P1 results in blue are displaced to the right. In general, models that

978 satisfy the solvability condition, the P1-E0 and P2-E1 models, are better behaved than the

979 P2-P1 model. This may be related to the well-known "weak" mass conservation of the

980 Taylor-Hood element that is greatly improved by enriching the pressure space with extra

981 pressures (Boffi et al., 2012).

982

June 27, 2025

983 **8. A Summary and Discussion**
984

985 In summary, this paper presents two innovations in ice sheet modeling. The first involves

986 a transformation of the ice sheet Stokes equations into a form that differs from the

987 approximate Blatter-Pattyn system by a small number of terms. In particular, the

988 variational formulations differ only by the absence of terms involving the vertical

989 velocity w in the second invariant of the strain rate tensor in the Blatter-Pattyn system.
990

991 We focus on two applications of the new transformation, although others may be

992 possible. The first allows these extra terms to be "switched" on or off to convert the code

993 from a full-Stokes model to a Blatter-Pattyn model if desired. Ice sheet flow is generally

994 shallow but often contains limited areas where Stokes equations must be solved. Thus,

995 the switch from Blatter-Pattyn to Stokes may be done locally and adaptively only where

996 the extra accuracy is required.
997

998 The fact that neglecting the vertical velocity in only one localized place creates

999 the Blatter-Pattyn approximation suggests that an improved approximation will result

1000 from approximating rather than neglecting the vertical velocity. We present two such

1001 approximations. but again others may be possible. The first approximation solves the

1002 pressure-free horizontal momentum equation with the vertical velocity obtained from the

1003 continuity equation. This approximation turns out to be the same as a model originally

1004 proposed by Herterich (1987). We therefore refer to it as the Herterich approximation.

1005 The second approximation is obtained by discretizing the continuity equation on a coarser

1006 mesh than that used by the rest of the model, which yields an approximate vertical

1007 velocity and thus an approximate Stokes model.
1008

1009 The second innovation involves the use of finite element discretizations that

1010 create a decoupled invertible continuity equation. This allows for the numerical solution

1011 of the vertical velocity in terms of the horizontal velocity components, i.e., $w = w(u,v)$,

1012 which makes these meshes a prerequisite for many of the applications mentioned above.

1013 Examples of such meshes for use in 2D and 3D are given in Appendix A, including the

1014 P1-E0 mesh that is used in most of the test problems of the paper. However, perhaps the

1015 most important consequence is that invertibility of the continuity equation serves as an

1016 alternative condition for well posedness of Stokes saddle point problems, as explained in

1017 Appendix B.

1018

1019 **Code Availability**

1020

1021 All calculations were made using the Wolfram Research, Inc. program Mathematica in a

1022 development environment. A large number of Mathematica Notebooks were used to

1023 produce the various results. A representative Notebook (a ,nb file) is available in a public

1024 repository at https://doi.org/10.5281/zenodo.13940989 for a Test $D*$ calculation

1025 (described in Appendix C) at $L = 10\,\text{km}$ and a resolution of 20x20. This test problem

1026 was chosen to demonstrate the use of direct substitution for the frictional tangential

1027 boundary condition, (16), in the functional. A Mathematica Notebook may be viewed by

1028 downloading the free Wolfram Player from https://www.wolfram.com/player/. However,

1029 the full Mathematica code is required for editing or execution.

1030

1031 **Competing Interests**

1032

1033 The author has acknowledged that there are no competing interests.

1034

1035 **Acknowledgements**

1036

1037 I am grateful to Mauro Perego, William (Bill) Lipscomb, and particularly to reviewer

1038 Prof. Christian Schoof, for comments and suggestions that helped to improve the paper.

1039

1040 **References**

1041

1042 Auricchio, F., da Veiga, L.B., Brezzi, F., and Lovadina, C.: Mixed Finite Element

1043 Methods, In Encyclopedia of Computational Mechanics Second Edition (Eds E. Stein, R.

1044 de Borst, and T.J.R. Hughes), John Wiley & Sons, Ltd., 2017.

1045

1046 Benzi, M., Golub, G.H., and Liesen, J.: Numerical Solution of Saddle Point Problems,

1047 Acta Numerica, 14 , 1-137, doi:10.1017/S0962492904000212, 2005.

1048

1049 Blatter, H.: Velocity and Stress Fields in Grounded Glaciers: A Simple Algorithm for

1050 Including Deviatoric Stress Gradients, J. Glaciol., 41, 333-344, 1995.

1051

June 27, 2025

1052 Boffi, D., Brezzi, F., Fortin, M.: Finite Elements for the Stokes Problem. In: Boffi D.,
1053 Gastaldi L. (eds) Mixed Finite Elements, Compatibility Conditions, and Applications.
1054 Lecture Notes in Mathematics, vol 1939. Springer, Berlin, Heidelberg.
1055 https://doi.org/10.1007/978-3-540-78319-0_2, 2008.

1056

1057 Boffi, D., Cavallini, N., Gardini, F., and Gastaldi, L.: Local Mass Conservation of Stokes
1058 Finite Elements, J. Sci. Comput., 52, 383–400, 2012.

1059

1060 Cheng, G., Lötstedt, P., and von Sydow, L.: A Full Stokes Subgrid Scheme in Two
1061 Dimensions for Simulation of Grounding Line Migration in Ice Sheets Using Elmer/ICE
1062 (v8.3), Geosci. Model Dev., 13, 2245-2258, 2020.

1063

1064 Colinge, J., and Rappaz, J.: A Strongly Nonlinear Elliptic Problem Arising in a Non-
1065 Newtonian Fluid Flow Model in Glaciology, Math. Model. Numer. Anal., 33, 395-
1066 406,1999.

1067

1068 Dukowicz, J.K., Price, S.F., and Lipscomb, W.H.: Consistent Approximations and
1069 Boundary Conditions for Ice Sheet Dynamics from a Principle of Least Action, J.
1070 Glaciol., 56, 480-496, 2010.

1071

1072 Dukowicz, J.K., Price, S.F., and Lipscomb, W.H.: Incorporating Arbitrary Basal
1073 Topography in the Variational Formulation of Ice Sheet Models, J. Glaciol., 57, 461-467,
1074 2011.

1075

1076 Elman, H.C., Silvester D.J., and Wathen A.J.: Finite Elements and Fast Iterative Solvers:
1077 With Applications in Incompressible Fluid Dynamics, 2nd Ed., Oxford University Press,
1078 494 pp, 2014.

1079

1080 Gagliardini, O., and Zwinger, T.: The ISMIP-HOM Benchmark Experiments Performed
1081 Using the Finite-Element Code Elmer, The Cryosphere, 2, 67–76, 2008.

1082

1083 Gagliardini, O., Zwinger, T., Gillet-Chaulet. F., Durand, G., Favier, L., de Fleurian, B.,
1084 Greve, R., Malinen, M., Martín, C., Råback, P., Ruokolainen, J., Sacchettini, M., Schäfer,
1085 M., Seddik, H., and Thies, J.: Capabilities and Performance of Elmer/Ice, a New-

1086   Generation Ice Sheet Model, Geosci. Model Dev., 6, 1299–1318, doi:10.5194/gmd-6-
1087   1299-2013, 2013.

1088

1089   Glowinski, R. and Rappaz, J.: Approximation of a Nonlinear Elliptic Problem Arising in
1090   a Non-Newtonian Fluid Flow Model in Glaciology, Math. Model. Numer. Anal., 37, 175-
1091   186, 2003.

1092

1093   Greve, R. and Blatter, H.: Dynamics of Ice Sheets and Glaciers, Springer-Verlag, Berlin
1094   Heidelberg, 301 pp, 2009.

1095

1096   Heinlein, A., Perego, M., and Rajamanickam, S.: FROSch Preconditioners for Land Ice
1097   Simulations of Greenland and Antarctica, SIAM J. Sci. Comput., 44, V339-B367, doi:
1098   10.1137/21M1395260, 2022.

1099

1100   Herterich, K.: On the Flow Within the Transition Zone Between Ice Sheet and Ice Shelf,
1101   in Dynamics of the West Antarctic Ice Sheet, Proceedings of a workshop held in Utrecht,
1102   May 6-8, 1985, (Eds. C. J. Van Der Veen and J. Oerlemans), D. Reidel, Dordrecht, 185-
1103   202, 1987.

1104

1105   Hoffman, M. J., Perego, M., Price, S. F., Lipscomb, W. H., Zhang, T., Jacobsen, D.,
1106   Tezaur, I., Salinger, A. G., Tuminaro, R., and Bertagna, L.: MPAS-Albany Land Ice
1107   (MALI): A Variable-Resolution Ice Sheet Model for Earth System Modeling Using
1108   Voronoi Grids, Geosci. Model Dev., 11, 3747–3780, doi:10.5194/gmd-11-3747-2018,
1109   2018.

1110

1111   Hood, P. and Taylor, C.: A Numerical Solution of the Navier-Stokes Equations Using the
1112   Finite Element Technique, Comput. Fluids, 1, 1-28, 1973.

1113

1114   Larour, E., Seroussi, H., Morlighem, M., and Rignot, E.: Continental scale, high order,
1115   high spatial resolution, ice sheet modeling using the Ice Sheet System Model (ISSM), J.
1116   Geophys. Res., 117, 1–20, doi:10.1029/2011JF002140, 2012.

1117

1118   Leng, W., Ju, L., Gunzburger, M., Price, S., and Ringler, T.: A Parallel High-Order
1119   Accurate Finite Element Nonlinear Stokes Ice Sheet Model and Benchmark Experiments,

June 27, 2025

1120   J. Geophys. Res., 117, 2156–2202, doi:10.1029/2011JF001962, 2012.

1121

1122   Lipscomb, W.H., Price, S.F., Hoffman, M.J., Leguy, G.R., Bennett, A.R., Bradley, S.L.,

1123   Evans, K.J., Fyke, J.G., Kennedy, J.H., Perego, M., Ranken, D.M., Sacks, W.J., Salinger,

1124   A.G., Vargo, L.J., and Worley, P.H.: Description and Evaluation of the Community Ice

1125   Sheet Model (CISM) v. 2.1, Geosci. Model Dev., 12, 387-424, 2019.

1126

1127   Nowicki, S.M.J. and Wingham, D.J.: Conditions for a Steady Ice Sheet-Ice Shelf

1128   Junction, *Earth Planet. Sci. Lett.,* **265**(1-2), 246-255, 2008.

1129

1130   Pattyn, F.: A New Three-Dimensional Higher-Order Thermomechanical Ice Sheet

1131   Model: Basic Sensitivity, Ice Stream Development, and Ice Flow across Subglacial

1132   Lakes, J. Geophys. Res., 108(B8), 2382, 2003.

1133

1134   Pattyn, F., Perichon, L., Aschwanden. A., Breuer, B., de Smedt, B., Gagliardini, O.,

1135   Gudmundsson, G.H., Hindmarsh, R.C.A., Hubbard, A., Johnson, J.V., Kleiner, T.,

1136   Konovalov, Y., Martin, C., Payne, A.J., Pollard, D., Price, S., Ruckamp, M., Saito, F.,

1137   Soucek, O., Sugiyama, S., and Zwinger, T.: Benchmark Experiments for Higher-Order

1138   and Full-Stokes Ice Sheet Models (ISMIP–HOM*),* The Cryosphere, 2, 95-108, 2008.

1139

1140   Perego, M., Gunzburger. M., and Burkardt, J.: Parallel Finite-Element Implementation

1141   for Higher-Order Ice-Sheet Models, J. Glaciol., 58, 76-88, 2012.

1142

1143   Rappaz, J., and Reist, A.: Mathematical and Numerical Analysis of a Three-Dimensional

1144   Fluid Flow Model in Glaciology, Math. Model. Mech. Appl. Sci., 15, 37-52, 2005.

1145

1146   Rückamp, M., Kleiner, T., and Humbert, A.: Comparison of ice dynamics using full-

1147   Stokes and Blatter-Pattyn approximation: application to the Northeast Greenland Ice

1148   Stream, The Cryosphere, 16, 1675-1696, 2022.

1149

1150   Schoof, C.: A Variational Approach to Ice Stream Flow, J. Fluid Mech., 556, 227-251,

1151   2006.

1152

June 27, 2025

Schoof, C.: Coulomb friction and other sliding laws in a higher order glacier flow model, Math. Models. Meth. Appl. Sci., 20(1), 157–189, 2010.

Schoof, C. and Hewitt, I.: Ice-Sheet Dynamics, Annu. Rev. Fluid Mech., 45, 217–239, 2013.

Schoof, C. and Hindmarsh, R.C.A.: Thin-Film Flows with Wall Slip: An Asymptotic Analysis of Higher Order Glacier Flow Models, Quart. J. Mech. Appl. Math, 63, *73-114*, 2010.

Seroussi, H., Ben Dhia, H., Morlighem, M., Latour, E., Rignot, E., and Aubry, D.: Coupling Ice Flow Models of Varying Orders of Complexity with the Tiling Method, J. Glaciol., 58, 776-786, 2012.

Tezaur, I. K, Perego, M., Salinger, A. G., Tuminaro, R. S., and Price, S. F.: Albany/FELIZ: A Parallel, Scalable and Robust, Finite Element, First-Order Stokes Approximation Ice Sheet Solver Built for Advanced Analysis, Geosci. Model Dev., 8, 1197-1220, 2015.

Appendix A: Meshes that Satisfy the Solvability Condition
A1 The P1-E0 Element and the Invertibility of the Continuity Equation

As discussed in §4, the invertibility of the discrete continuity equation requires special elements and meshes that satisfy the solvability condition (58). One such element illustrated in Fig. A1, the P1-E0 element, has been used on many of the problems in this paper. To work well for inverting the continuity equation for the vertical velocity, i.e., (56), it must be used in a mesh composed of vertical columns subdivided into triangular elements as illustrated in a representative mesh shown in Fig. A2. Element P1-E0 has velocities located at triangle vertices for a linear velocity distribution within each triangle (P1), and pressure located on the vertical edge of each triangle for a constant pressure distribution over the two triangles that share the edge (E0). A second order version of this element, the P2-E1 element, is shown in Fig. 13A.

June 27, 2025

1185
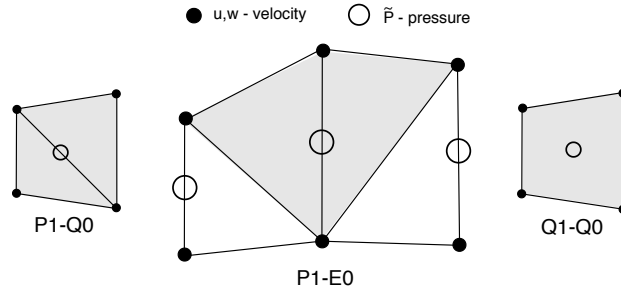
1186   **Figure A1.** The P1-E0 element, and two other secondary 2D elements that satisfy

1187   the solvability condition but possibly only in Tests B and D[*].

1188

1189
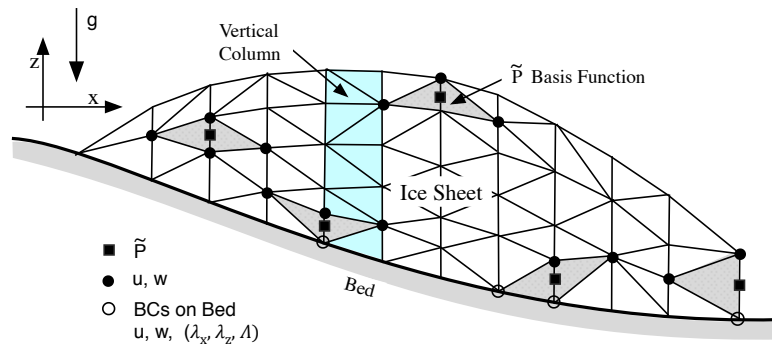
1190   **Figure A2.** An illustration of a 2D edge-based P1-E0 mesh, composed of

1191   vertical columns randomly subdivided into triangles.

1192

1193   The triangulation and the configuration of pressure basis functions (shown in

1194   gray) in Fig. A2 is quite general, except that elements need to be arranged in vertical

1195   columns, which still allows for a flexible triangulation of an arbitrary domain. Generally,

1196   there are two triangles associated with a pressure variable, one on each side of a vertical

1197   edge, except where the ice sheet ends at a vertical face, as in Fig. A2. However, this is

1198   not a problem since the pressure is simply associated with the single triangle on one side

1199   of the vertical face. Meshes composed of P1-E0 elements have another useful property.

1200   Since pressure and vertical velocity variables alternate along vertical mesh lines, the

1201   matrix-vector products $\mathbf{M}_{WP}p$, $\mathbf{M}_{WP}^{T}w$ in (46), corresponding to $\partial\tilde{P}/\partial z$ and $\partial w/\partial z$ in

1202   the vertical momentum and continuity equations, respectively, produce simple decoupled

1203   bi-diagonal one-dimensional difference equations along each vertical mesh line for

1204   determining the pressure and vertical velocity. This is particularly advantageous for

1205   parallelization purposes.

1206

1207   The other two elements shown in Fig. A1, the P1-Q0 and Q1-Q0 elements, are not

1208   as general. They satisfy the solvability condition when used in Tests B and D[*] but

1209   possibly not in other problems. The P1-Q0 element has velocities on triangle vertices for

1210   a linear velocity distribution within each triangle (P1) but pressure is constant within the

1211   quadrilateral (Q0) formed by the two adjoining triangles. The Q1-Q0 element has

1212   velocities located at quadrilateral vertices and pressure centered in the quadrilateral,

1213   resulting in a bi-quadratic velocity distribution (Q1) and a constant pressure within the

1214   quadrilateral (Q0). Solutions for all three elements are stable as expected, and they

1215   produce the correct value for ice transport. The pressure distribution is smooth in the P1-

1216   E0 case but contains small fluctuations near the upper surface in the P1-Q0 and Q1-Q0

1217   cases. These disappear as resolution is increased. The Q1-Q0 element is unstable in

1218   conventional applications because it contains a checkerboard pressure null space and is

1219   only used in a stabilized form (see Elman et al., 2014, where the element is called Q1-

1220   P0). Here, however, it behaves well, presumably because it satisfies the solvability

1221   condition. Overall, this confirms our expectation of stability when the solvability

1222   condition is satisfied.

1223

1224   **A2 Proving the Solvability Condition in P1-E0 Element Meshes**

1225

1226   Consider a single vertical edge from top to bottom as in Fig. A2. Assuming m

1227   vertical edge segments, there will be $m+1$ discrete w variables and m discrete p

1228   variables since each p variable is located between a pair of w variables. However, since

1229   the w variable at the bottom is specified as a boundary condition, either as a no-slip

1230   condition or as a no-penetration condition, there will be only m unknown w variables.

1231   As a result, we have $n_w = n_p$ along each vertical mesh edge, and therefore over the entire

1232   mesh, thus satisfying the solvability condition. In case Lagrange multipliers are used,

1233   there will be $m+1$ unknown discrete w variables (since now the basal vertical velocity

1234 w is an unknown). However, this is matched by m unknown p variables, supplemented

1235   by one λ_z or one Λ unknown Lagrange multiplier variable, depending on the type of

1236   boundary condition. Thus, the number of unknown variables again equals the number of

1237   equations along every vertical edge, thereby satisfying the solvability condition. This

1238   means that the P1-E0 element can be used to satisfy the solvability condition irrespective

1239   of the boundary conditions on arbitrary meshes. These arguments will apply to other

June 27, 2025

1240   versions of the P1-E0 element as well, such as the second order version P2-E1 in Fig.

1241   13A or the 3D version of the P1-E0 element in Fig. A3.

1242

1243   **A3 Three-Dimensional Meshes Based on the P1-E0 Element**

1244

1245   The two-dimensional P1-E0 element has a relatively simple three-dimensional

1246   counterpart, shown in Fig. A3. The mesh again consists of vertical columns, this time

1247   composed of hexahedra. Each hexahedron is subdivided into six tetrahedra such that

1248   each vertical edge is surrounded by as few as four to as many as eight tetrahedra. As in

1249   the 2D case, velocity components are collocated at vertices, yielding a piecewise-linear

1250   velocity distribution in each tetrahedral element, and pressures are located in the middle

1251   of each vertical edge so that pressure is constant in the collection of tetrahedra that

1252   surround that edge. Lagrange multipliers, if used, are located at the vertices on the basal

1253   surface, yielding a piecewise linear distribution on the basal triangular facet. The

1254   solvability condition (58) is satisfied because the argument used in the 2D case applies

1255   here also since pressures and vertical velocities are again intermingled along a single line

1256   of vertical edges from top to bottom.

1257
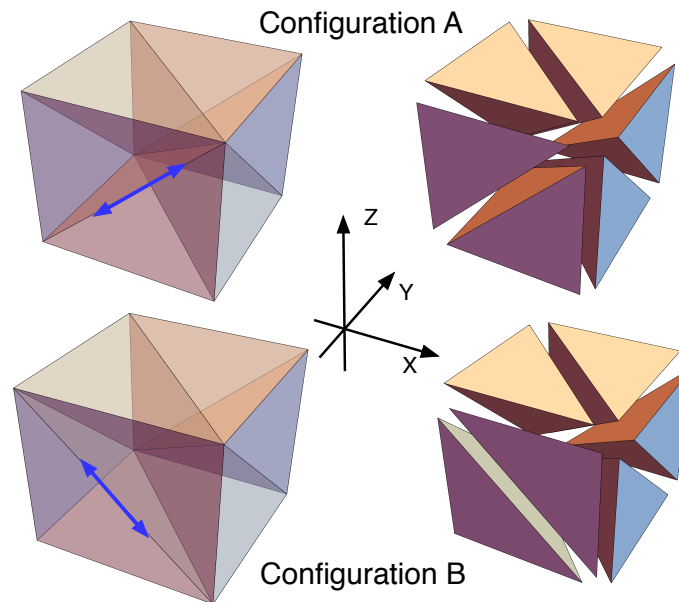
1258   **Figure A3.** Three-dimensional P1-E0 tetrahedral elements that generalize the 2D P1-E0

1259   element of Fig. A1. Configurations A and B differ by having an internal triangular

1260   face rotated, as indicated by the blue arrows. Both satisfy the solvability condition.

1261

1262   Fig. A3 shows two of the several possible configurations of a typical hexahedron,

1263   including an exploded view of each configuration for clarity. The two configurations

1264 differ in having the internal face of the two forward-facing tetrahedra rotated, creating

1265 two different forward facing tetrahedra. The remaining six tetrahedra are undisturbed.

1266 Since edges must align when hexahedra (or tetrahedra) are connected, this shows that the

1267 3D mesh can be flexibly reconnected and rearranged, just as in the 2D case of Fig. A2.

1268

1269   A closely related and perhaps simpler three-dimensional P1-E0 element is based

1270 on a P2-P1 prismatic tetrahedral element discussed in Leng et al. (2012). A mesh of

1271 these elements is composed of vertical columns of prisms (with triangular faces at the top

1272 and bottom), each subdivided into three tetrahedra. Pressures are located on the vertical

1273 prism edges, as in Fig. A3, so this again satisfies the solvability condition.

1274

1275   Just as the 2D second-order P2-E1 element in Fig. 13A is a generalization of the

1276 P1-E0 element, a 3D second-order P2-E1 element may be constructed as a generalization

1277 of the P1-E0 element of Fig. A3. Velocities would be located at the vertices and at

1278 midpoints of the tetrahedral edges, and pressures halfway between the velocities on

1279 vertical edges, including a set of imaginary vertical edges through the midpoints of the

1280 tetrahedral edges as in the 2D case in Fig. 13A. The P2-E1 element in both 2D and 3D

1281 will again satisfy the solvability condition since the arguments of §B2 will also apply as

1282 pressures are located midway between vertical velocities along all vertical edges.

1283

1284 **Appendix B: The Inf-Sup and Solvability Conditions**

1285

1286 Recalling (47), the 2D Newton-Raphson iteration for saddle point problems is written as

1287
$$
\begin{bmatrix}
\mathbf{M}_{UU}\left(u^K,w^K\right) & \mathbf{M}_{UW}\left(u^K,w^K\right) & \mathbf{M}_{UP} \\
\mathbf{M}_{UW}^T\left(u^K,w^K\right) & \mathbf{M}_{WW}\left(u^K,w^K\right) & \mathbf{M}_{WP} \\
\mathbf{M}_{UP}^T & \mathbf{M}_{WP}^T & 0
\end{bmatrix}
\begin{Bmatrix}
\Delta u \\
\Delta w \\
\Delta p
\end{Bmatrix}
=
\begin{Bmatrix}
-R_U\left(u^K,w^K,p^K\right) \\
-R_W\left(u^K,w^K,p^K\right) \\
0
\end{Bmatrix}.
\quad (71)
$$

1288 In 3D the vector Δu will include the two horizontal increments, i.e., $\Delta u \rightarrow \left\{\Delta u, \Delta v\right\}^T$.

1289 For simplicity, if we rename quantities, (71) may be put in the standard form (54) as

1290 follows

1291
$$
\begin{bmatrix}
\mathbf{A} & \mathbf{B}^T \\
\mathbf{B} & 0
\end{bmatrix}
\begin{Bmatrix}
\mathbf{u} \\
p
\end{Bmatrix}
=
\begin{Bmatrix}
\mathbf{f} \\
g
\end{Bmatrix},
\quad (72)
$$

June 27, 2025

1292 where $\mathbf{u} = \{\Delta u, \Delta w\}^T$, $\mathbf{A} = \begin{bmatrix} \mathbf{M}_{UU}(u^K, w^K) & \mathbf{M}_{UW}(u^K, w^K) \\ \mathbf{M}_{UW}^T(u^K, w^K) & \mathbf{M}_{WW}(u^K, w^K) \end{bmatrix}$, $\mathbf{B} = \begin{bmatrix} \mathbf{M}_{UP}^T & \mathbf{M}_{WP}^T \end{bmatrix}$, and

1293 similarly for other variables.

1294

1295   As noted earlier, matrix $\mathbf{A}$ is invertible. Solving for and eliminating $\mathbf{u}$ in (72),

1296 one obtains an equation for the pressure,

$$\left(\mathbf{B}\mathbf{A}^{-1}\mathbf{B}^T\right)p = \left(\mathbf{B}\mathbf{A}^{-1}\right)\mathbf{f} , \tag{73}$$

1297

1298 where $\mathbf{S} = \left(\mathbf{B}\mathbf{A}^{-1}\mathbf{B}^T\right)$ is the Schur complement with respect to p. This equation may be

1299 solved for p provided an inf-sup condition on matrix $\mathbf{B}^T$ is satisfied (Benzi et al., 2005;

1300 and more specifically see the lecture notes by Prof. J-F. Gerbeau for Course CME358,

1301 Stanford University, Chapter 3 (in particular Remarks 3.2 and 3.3), available in:

1302 https://web.stanford.edu/class/cme358/notes/cme358_lecture_notes_3.pdf). Having

1303 solved for p, the velocity $\mathbf{u}$ is obtained as follows

$$\mathbf{u} = \mathbf{A}^{-1}\left(\mathbf{f} - \mathbf{B}^T p\right). \tag{74}$$

1304

1305 This is generally not a practical solution method since the Schur complement matrix $\mathbf{S}$ is

1306 dense and therefore it is too expensive to solve (73). In particular, Gerbeau shows that

1307 the standard inf-sup condition for $\mathbf{B}^T$ is equivalent to the much simpler condition,

$$Ker\mathbf{B}^T = \{0\} , \tag{75}$$

1308

1309 which is called the "algebraic inf-sup condition". In other words, the inf-sup condition is

1310 equivalent to requiring the null space of $\mathbf{B}^T$ to be the zero vector, which means that the

1311 solution for pressure must not contain spurious modes. This suggests that the existence

1312 of a pressure null space is the culprit in the need to satisfy the inf-sup condition.

1313

1314   Now consider the situation when the Newton-Raphson system (71) is solved with

1315 a mesh satisfying the solvability condition. Simplifying notation as before, the linear

1316 system (71) may be written as follows

1317
$$\begin{bmatrix} \mathbf{M}_{UU} & \mathbf{M}_{UW} & \mathbf{M}_{UP} \\ \mathbf{M}_{UW}^T & \mathbf{M}_{WW} & \mathbf{M}_{WP} \\ \mathbf{M}_{UP}^T & \mathbf{M}_{WP}^T & 0 \end{bmatrix} \begin{Bmatrix} u \\ w \\ p \end{Bmatrix} = \begin{Bmatrix} f_U \\ f_W \\ 0 \end{Bmatrix} . \tag{76}$$

1318 As shown in §4.3.2, if the solvability condition applies then matrices $\mathbf{M}_{WP}, \mathbf{M}_{WP}^T$ are

1319 invertible, and the continuity equation, the third equation in (76), may be solved for the

1320 vertical velocity w, as in (56). Using (56) in the functional (59) one obtains (60), an

1321 equation for u only. With a bit of algebra, and using (56) in (76), the corresponding

1322 linear equation for u is given by

1323
$$\left(\mathbf{M}_{UU} - \left(\mathbf{M}_{UW} - \mathbf{M}_{UP}\mathbf{M}_{WP}^{-1}\mathbf{M}_{WW}\right)\mathbf{M}_{WP}^{-T}\mathbf{M}_{UP}^T - \mathbf{M}_{UP}\mathbf{M}_{WP}^{-1}\mathbf{M}_{UW}^T\right)u$$
$$= \left(f_U - \mathbf{M}_{UP}\mathbf{M}_{WP}^{-1}f_W\right). \tag{77}$$

1324 As pointed out in §4.3.2, this is a well-behaved and stable equation for u. However, just

1325 as was the case with (73), the associated matrix is dense and too expensive to solve in

1326 practice. Nevertheless, with u obtained from solving (77), the second equation of (76)

1327 yields the following matrix equation to be solved for the pressure p,

1328
$$\mathbf{M}_{WP}p = \left(\mathbf{M}_{WW}\mathbf{M}_{WP}^{-T}\mathbf{M}_{UP}^T - \mathbf{M}_{UW}^T\right)u + f_W. \tag{78}$$

1329 Thus, corresponding to equations (74) and (73), one obtains equations (77) and (78), but

1330 this time to be solved in reverse order, first for velocity u, then for the pressure p. The

1331 essential difference between the equations for pressure, (73) and (78), is that in (73) the

1332 Schur complement matrix $\mathbf{S}$ requires the inf-sup condition to be satisfied, while in (78)

1333 there is no such requirement for matrix $\mathbf{M}_{WP}$. Thus, pressure solutions will be well

1334 behaved with no spurious pressure modes, although there is no guarantee or expectation

1335 of smoothness. This implies that the solvability condition (58), and more importantly, the

1336 invertibility of matrix $\mathbf{M}_{WP}^T$, is sufficient for the well posedness of the Stokes saddle point

1337 problem.

1338

1339 **Appendix C: Test Problems**

1340

1341 We shall use three 2D test problems to demonstrate the new methods. The geometrical

1342 configuration of the three problem meshes is illustrated in Fig. C1. The first problem,

1343 named Test B, is actually Exp. B from the ISMIP-HOM benchmark suite (Pattyn et al.,

1344 2008); it features a no-slip condition on a sinusoidal basal surface. The second problem,

1345 Test D*, incorporates sinusoidal friction along a uniformly sloped plane basal surface.

1346 This is a modification of Exp. D from the benchmark suite but with increased friction

1347 since ice flow in Exp. D is very nearly vertically constant (see Fig. 4) that is characteristic

1348 of the shallow-shelf regime that is not of present interest.

ISMIP-HOM Test Problem B - No Slip

Test Problem D* - Sinusoidal Friction

Test Problem O - 20% Obstacle - No Slip

1349
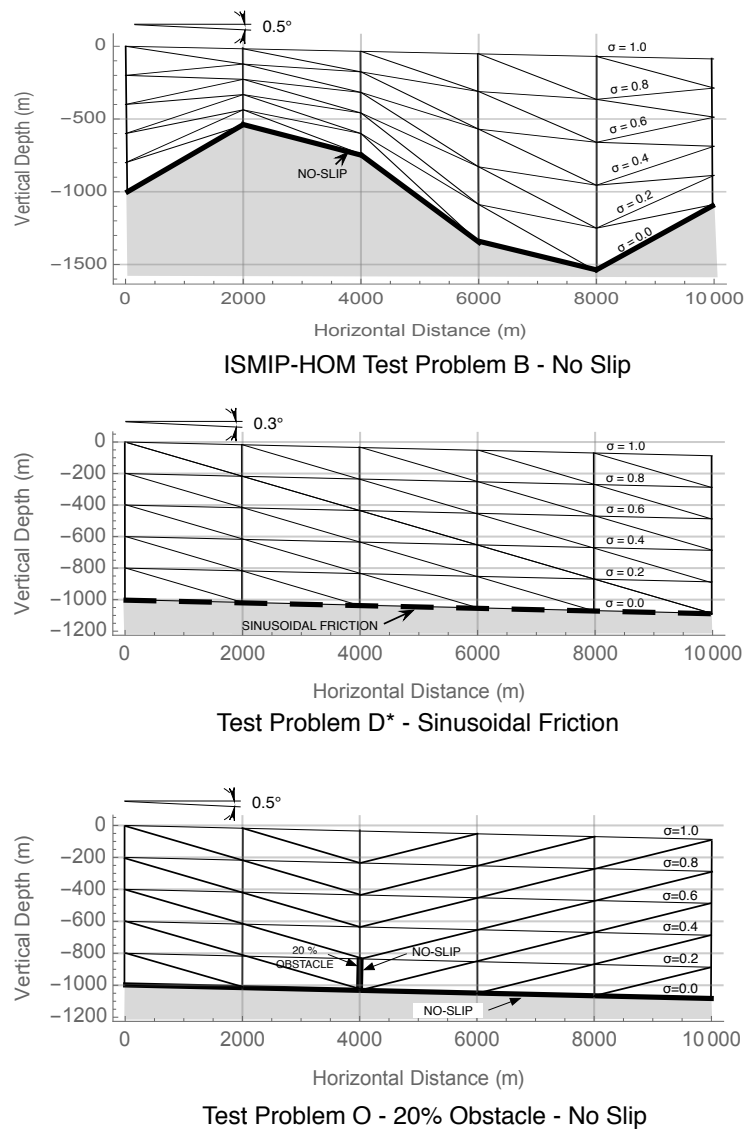
1350   **Figure C1.** Test problem meshes. For clarity, a coarse 5x5 configuration is shown.

1351

1352   A third problem, Test O (for "Obstacle") is introduced to illustrate the adaptive

1353 switching discussed in §6.1. As illustrated in Fig. C1, Test O has a unique feature, a thin

1354 no-slip obstacle, located at $x = 4\ km$ and extending vertically $200\ m$ from the bed (20 %

1355 of the ice sheet thickness), which forces ice flow near the obstacle to adjust abruptly.

1356 However, there is a problem if a triangulation like the one in Tests B or D* were to be

1357 used. This is because the no-slip boundary conditions in the triangular element in the lee

1358 of the obstacle, with one vertical edge and one edge along the bed, would result in all

1359 vertex velocities being zero. This would imply zero stress and therefore a singularity in

1360 ice viscosity. To avoid this, elements at the back of the obstacle are "reversed" compared

1361 to the ones at the front of the obstacle, as shown in Fig. C1.

June 27, 2025

1362

1363   All tests feature a sloping flat upper surface, given by $z_s(x) = -x\operatorname{Tan}(\theta)$, where

1364 $\theta = 0.5°$ for Tests B and O, and $\theta = 0.3°$ for Test D* (this is different from the $0.1°$ slope

1365 in Test D), with free-stress boundary conditions. The bottom surface elevation in Test B

1366 is given by $z_b(x) = z_s(x) - H_0 + H_1\operatorname{Sin}(\omega x)$, where the $H_0 = 1000\,m$, $H_1 = 500\,m$,

1367 $\omega = 2\pi/L$, and L is the perturbation wavelength or the domain length. The length L in

1368 the ISMIP-HOM suite ranges from $5\,km$ to $160\,km$ but here we consider only three

1369 cases at the high end of the aspect ratio (H_0/L) range, namely $L = 2, 5, 10\,km$, where the

1370 inaccuracy of the Blatter-Pattyn approximation becomes noticeable. The bottom surface

1371 elevation in Tests D* and O is $z_b(x) = z_s(x) - H_0$, parallel to the upper surface. The

1372 spatially varying friction coefficient for Test D* is $\beta(x) = \beta_0 + \beta_1\operatorname{Sin}(\omega x)$, where

1373 $\beta_0 = \beta_1 = 10^4\,Pa\,a\,m^{-1}$ (this is an order of magnitude larger than in Test D). Lateral

1374 boundary conditions are periodic. Physical parameters are the same as in ISMIP-HOM,

1375 i.e., ice-flow parameter $A = 10^{-16}\,Pa^{-3}a^{-1}$, ice density $\rho = 910\,kg\,m^{-3}$, and gravitational

1376 constant $g = 9.81\,ms^2$. In general, units are MKS, except time is usually per annum,

1377 convertible to per second by the factor $3.1557 \times 10^7\,s\,a^{-1}$.